ISSN 0030-400X, Optics and Spectroscopy, 2019, Vol. 127, No. 2, pp. 293–313. © Pleiades Publishing, Ltd., 2019.

NONLINEAR OPTICS

Low- and High-Order Nonlinear Optical Characterization of Metal Sulfide Quantum Dots

R. A. Ganeev*

The Guo China–US Photonics Laboratory, Changchun Institute of Optics, Fine Mechanics and Physics, Chinese Academy of Sciences, Changchun, 130033 China

**e-mail: rashid_ganeev@mail.ru*

Received March 7, 2019; revised March 7, 2019; accepted March 22, 2019

Abstract—Any new synthesized semiconductor nanoparticles or quantum dots (QDs) require to be examined under different conditions using laser pulses of variable energies, wavelengths and durations to understand the nonlinear optical mechanisms and distinguish their attractive properties for practical applications. Among various QDs, the metal sulfides took special attention due to their advanced nonlinear optical properties. Additionally, laser ablation can readily produce plasmas containing QDs that could be used for different applications. One of them is that they can be used as emitters for harmonic generation from ultrashort laser pulses. Here we review recent studies of different low- and high-order optical nonlinearities of metal sulfide QDs, such as optical limiting, two-photon, saturable and reverse saturable types of nonlinear absorption, nonlinear refraction, and generation of high-order harmonics in extreme ultraviolet range.

Keywords: nonlinear optics, metal sulfide quantum dots

DOI: 10.1134/S0030400X19080113

1. PERSPECTIVES OF METAL SULFIDE QUANTUM DOTS IN NONLINEAR OPTICS

The interest in small-sized species like quantum dots (QDs) is caused by enhancement of the nonlinear optical (NLO) response near their surface plasmon resonances [1]. The variation of quantum size effect in QDs can be achieved by doping with other semiconductor materials. The tuning of band gap energy of QDs without changing their size can be achieved by varying the alloyed QDs composition. This opportunity has spurred the fabrication of several varieties of alloyed QDs (CdSeTe, CdZnS, ZnCdSe, and CdSSe) with tunable optical properties [2]. Those alloyed semiconductor QDs with both homogeneous and gradient internal structures have been developed to achieve continuous tuning of the optical properties without changing the particle size.

Optical limiting (OL) is one of the potential applications of the materials' optical nonlinearities. It aimed in protecting eyes and sensitive registration devices from damaging. Previously, small-sized species, like nanoparticles and QDs, have shown the advantages in their use for OL [3, 4]. Among various QDs the metal sulfides took special attention due to their advanced NLO properties. Silver sulfide is the most studied QD sample [5]. NLO characterization of these QDs has revealed that, in the 532 nm spectral region, it possesses large nonlinear refraction and nonlinear absorption. The structure of those QDs, their Z-scans and the pump-probe characterization has been reported in numerous studies. Other most frequently studied metal sulfide samples include CdS and ZnS QDs. Those species showed large nonlinear refractive indices (γ) and nonlinear absorption coefficients (β) depending on the conditions of experiments [6, 7]. The development of the principles of formation of metal sulfide QDs with desired low-order NLO properties for different applications, particularly for generation of coherent extreme ultraviolet radiation through high-order harmonic generation during propagation of ultrashort pulses through the plasmas containing such QDs, is one of important tasks of nonlinear optics.

Silver sulfide is an attractive low band gap (E_g = 0.9 eV) semiconductor material. Due to its excellent optical and electronic properties Ag_2S has promising applications as a material with large NLO coefficients. The rapid development of such NLO materials, they still cannot meet the requirements for practical applications. One possible way to improve NLO response of materials is to modify their structure [8, 9]. Alongside the unique NLO properties of nanoparticles and nanostructures there is a continuously growing interest induced by the influence of the size and shape of these nanoparticles. Moreover, the existence of surface plasmon resonance (SPR) in nanoparticles has always been useful for the realization of strong NLO response upon interaction with intense laser pulses.

A search for new applications of QDs is an important task for optical community. The interesting idea is to find the optimal conditions in application of such QDs as effective emitters of the high-order harmonics of femtosecond pulses for development of efficient source of coherent extreme ultraviolet radiation. To date a large number of experiments with gas clusters and nanoparticles as well as ablated nanoparticles was conducted. Qualitative assessments show that the application of a group of particles containing a few thousand atoms is the most optimal for the maximum increase in the number of generated harmonic photons. The knowledge of the nonlinear absorptive and refractive properties of those small-sized structures [10–12] will allow definition of the optimal conditions of excitation of QDs for high-order harmonic generation (HHG) during formation of plasma plumes containing such species [13, 14]. The practical aspects of these studies include formation conditions for efficient emission of coherent extreme ultraviolet (XUV) radiation through HHG with further applications in different fields of physics, chemistry, and biology. The enhanced harmonic generation has been demonstrated using clusters and nanoparticles in the cases of gas HHG [15–18] and plasma HHG [19–21].

This review is organized as follows. In Section II, we analyze OL in the $Cd_{0.5}Zn_{0.5}S$ + erythrosine associates dissolved in water. We discuss the measurements of γ and β at different combinations of QD + dye associates using infrared and visible laser pulses of picosecond duration. In Section III, large nonlinear absorption ($\beta \approx 10^{-3}$ cm W^{-1}) of silver sulfide quantum dots at $\lambda = 400$ nm is analyzed. We discuss the properties of 4 nm Ag_2S QDs, which had been synthesized by a chemical method. Variations of the sign of nonlinear refractive indices and nonlinear absorption coefficients of QDs will be analyzed by different methods. Finally, in Section IV, HHG in such QDs using electronically driven delays between the heating and driving lasers is analyzed. Ag_2S, CdS, and ZnS QDs were ablated using a nanosecond laser, which allowed demonstration of efficient HHG in plasmas using a femtosecond laser. With this approach, effective harmonics generation in the spectral range from 20 to 115 nm using such QDs has been achieved.

2. OPTICAL LIMITING, NONLINEAR REFRACTION, AND NONLINEAR ABSORPTION OF THE ASSOCIATES OF $Cd_{0.5}Zn_{0.5}S$ QUANTUM DOTS AND DYES

2.1. Motivation of Studies and Experimental Arrangements

NLO studies of $CdSe_{0.8}S_{0.2}$ QDs using the Nd:YAG laser second harmonic radiation (λ = 532 nm, t = 35 ps) were reported in [22]. Those studies have shown that $CdSe_{0.8}S_{0.2}$ QDs possess strong reverse saturable absorption (RSA) and weak saturable absorption (SA), while the nonlinear absorption coefficient was measured to be three orders of magnitude larger than that of CdSeS-doped glasses. In [23], similar studies were reported using 532 nm nanosecond laser pulses. The composition-dependent NLO properties of $CdSe_xS_{1-x}$ alloyed QDs were analyzed by the Z-scan technique using 532 nm laser radiation [24]. The 4 to 10 fold growth of NLO characteristics, particularly two-photon absorption (2PA), in $CdSe_xS_{1-x}$ depending on x values (from 0 to 1) has been shown.

The aqueous synthesis of mixed cadmium and zinc sulfide colloidal QDs has been successfully realized and the method for preparation of colloidal $Cd_xZn_{1-x}S$ QDs in a cubic crystal lattice with particle size of ~2 nm has been demonstrated in [25]. In those studies the blue shift of optical absorption maximum from 420 to 295 nm and the recombination photoluminescence from 646 to 483 nm with increasing zinc content in QDs was observed. Those results have prompted the preparation of CdZnS QDs films and the studies of the photoluminescence properties of CdZnS QD suspensions for solar cells applications. Meanwhile, one can note the absence of OL studies of alloyed $Cd_{1-x}Zn_xS$ QDs and its associates with various molecules in the visible range. Notice that these monodisperse wurtzite nanoalloys possess superior optical properties with photoluminescence quantum yields of 25–50% [26].

The absorption spectra of synthesized $Cd_{1-x}Zn_xS$ reveal that their optical band gaps are in good agreement with the values found by calculating the interband emission energy [27]. It was predicted that investigation of $Cd_{1-x}Zn_xS$ QDs and their associates with molecules, such as dyes, will prompt the application of the attractive properties of those alloyed metal sulfide multiatomic materials in the future. The interest in such QD-containing systems has been increased during last time due to expectations for simultaneous application of the attractive properties of each of components for different potential applications. Moreover, QDs associated with different dyes may further amend the optical and NLO response of newly developed species. In this connection $Cd_{1-x}Zn_xS$ QDs associates with organic dyes may demonstrate the advanced OL in the visible range. One has to carefully analyze different conditions of the formation of such associates from the point of view of their advanced OL properties, as well as to study their NLO characteristics, such as γ, β, 2PA, SA, and RSA.

Below we review the optical limiting, nonlinear refraction and nonlinear absorption studies of the associates of $Cd_{0.5}Zn_{0.5}S$ quantum dots and dyes [28]. The preparation of zinc-cadmium sulfide QDs in gelatin was described in [25]. The concentration of QDs was equal to 2% of mass of gelatin. Associates were prepared by mixing the water solutions of dyes and QDs at the molar ratio of 0.03 : 1.

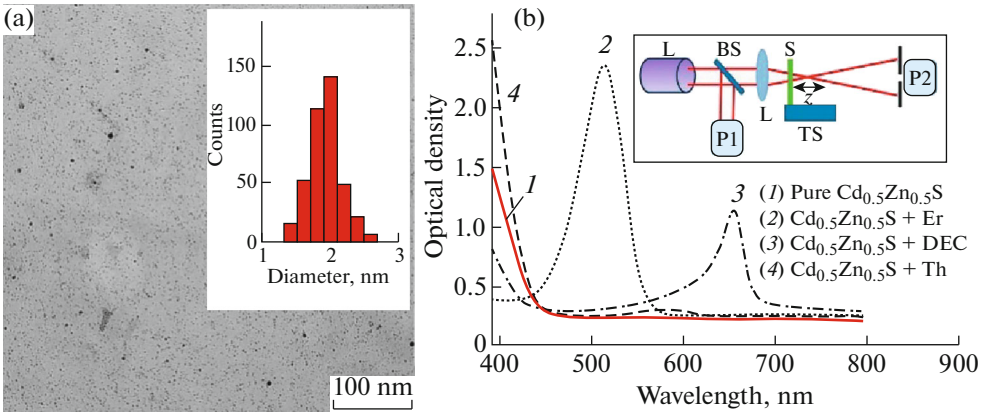

Fig. 1. (a) TEM and histogram of the size distribution of $Cd_{0.5}Zn_{0.5}S$ QDs. (b) Absorption spectra of $Cd_{0.5}Zn_{0.5}S$ QDs and QDs + dyes in water. (*1*) $Cd_{0.5}Zn_{0.5}S$ QDs in water; (*2*) $Cd_{0.5}Zn_{0.5}S$ QDs + erythrosine (Er) in water; (*3*) $Cd_{0.5}Zn_{0.5}S$ QDs + DEC in water; (*4*) $Cd_{0.5}Zn_{0.5}S$ QDs + thionine (Th) in water. Inset: experimental scheme for Z-scan measurements. LASER, Nd:YAG laser; BS, beamsplitter; PD1, PD2, photodiodes; FL, focusing lens; S, sample; TS, translating stage. Reproduced from [28].

Transmission electron microscopy (TEM) image of QDs is shown in Fig. 1a. The mean size of $Cd_{0.5}Zn_{0.5}S$ QDs was about 2 nm (see inset). The absorption spectra of $Cd_{0.5}Zn_{0.5}S$ QDs and its associates with dyes are shown in Fig. 1b. Three dyes of different classes (thiazine (thionine), xanthene (erythrosine), and carbocyanine (3,3'-di-(γ-sulfopropyl)–4,4',5,5'–dibenzo-9–ethylthiacarbocyaninebetaine pyridinium salt; further this dye will be dubbed as DEC)) were used as the associative molecules. These dyes were chosen to change the linear absorption peaks of the mixtures of $Cd_{0.5}Zn_{0.5}S$ QDs + dyes near the wavelength of the second harmonic (532 nm) of Nd:YAG laser radiation.

NLO processes in QD + dye associates were analyzed at the wavelengths of 1064 nm and 532 nm using picosecond pulses. The experimental set-up contained the picosecond Nd:YAG laser, which generated a single pulse ($\tau = 40$ ps) at 2 Hz repetition rate and closed-aperture (CA) and open-aperture (OA) Z-scan schemes for NLO characterization of associates. Laser radiation ($\lambda = 1064$ nm), or its second harmonic ($\lambda = 532$ nm) generated in KDP crystal, was focused by a 25 cm focal length lens (see inset in Fig. 1b). The beam waist diameters were 80 μm and 60 μm (at half width of $1/e^2$ maximum of the spatial distribution at the focal plane) in the case of fundamental and second harmonic beams respectively. The 2-mm-thick fused silica cells containing QDs or QD + dye associates were moved along the *z*-axis through the focal point using a translating stage controlled by a computer. The intensities of the optical breakdown of QD + dye associates were measured to be 2.5×10^{11} W cm^{-2} and 1×10^{11} W cm^{-2} at the wavelengths of the fundamental and second harmonic radiation respectively, while the maximum intensities of radiation in the experiments did not exceed 1×10^{11} W cm^{-2} (1064 nm) and 3×10^{10} W cm^{-2} (532 nm). OL studies were carried out by varying the energy of the pulses propagating through the cells. The energy was changed using the calibrated filters. The sample was placed on the path of focused radiation at the position when energy density was sufficient for observation of optical limiting.

2.2. Optical Limiting and Z-scans of QD + Dye Associates

OL was analyzed using the 532 nm, 40 ps pulses propagated through the $Cd_{0.5}Zn_{0.5}S$ QDs + erythrosine associates in water. This solution was placed close to the focal plane of 400 mm focal length lens. The energy of 532 nm pulses was gradually increased and measured the output radiation propagated through the 1-mm-thick cell contained QD + dye associates. The linear dependence between input and output pulses was maintained up to the input pulse energy of ~1.1 mJ (Fig. 2). Further grow of input pulse energy led to OL of the energy of propagated laser radiation (filled circles).

This process was maintained up to the maximal available energy of 532 nm pulses (~2.5 mJ), which allowed stabilization of output energy at the level of 0.65 mJ along the 1.1–2.5 mJ energy range of input pulses. Note that OL effect has previously been reported in different dyes [29] and the competitive contribution of SA, as well as joint influence of 2PA and RSA, on OL in thionine was analyzed.

In discussed studies, the contribution of QDs on OL in QD + dye associates played a decisive role, since at high pulse energies the joint influence of 2PA and RSA becoming stronger than the influence of SA. Similar conclusion has been reported in [30], which have shown that OL in CdSe QD was based on RSA.

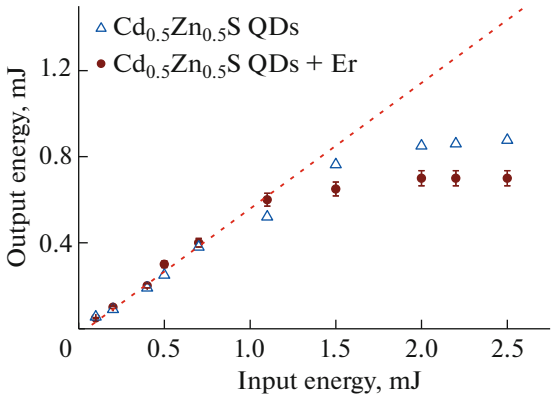

Fig. 2. Optical limiting of 532 nm, 40 ps pulses in the water solution contained $Cd_{0.5}Zn_{0.5}S$ QDs without dyes (blue empty triangles) and $Cd_{0.5}Zn_{0.5}S$ QDs + erythrosine associates (red filled circles). Reproduced from [28].

This process dominated over SA at higher intensities of 532 nm laser radiation. OL in QD + dye associates discussed in present review was also mostly attributed to RSA. OL occurred at the pulse energy much higher than the energy of laser radiation at which SA became a dominating process at similar focusing conditions (1.1 and 0.1 mJ, respectively).

Similar, though less pronounced, OL properties were observed in QD + thionine and QD + DEC associates. As for QD water solution without dyes, OL was observed at narrower range of limitation of the output pulses (1.5–2.5 mJ). In the case of QD + erythrosine, ~2.1 fold decrease of output pulse energy compared with input radiation was achieved. One can compare the expected energy of output pulses without limiting effect depicted from the dashed line (~1.4 mJ) and actual energy of those pulses (0.65 mJ, Fig. 2) at the input pulse energy of 2.5 mJ. At similar conditions, pure QDs in water showed the ~1.8 fold decrease of output energy (Fig. 2, empty triangles). These observations point out the relative influence of dye molecules attached to QDs on OL properties of QD + dye associates.

To quantitatively analyze different NLO processes responsible for OL in QDs and QD + dye associates, one has to measure γ and β using standard Z-scan technique. Below we discuss the results of those studies. The Z-scans showing normalized transmittances of $Cd_{0.5}Zn_{0.5}S$ QDs in water using 1064 and 532 nm pulses are presented in Fig. 3. The $Cd_{0.5}Zn_{0.5}S$ QD-containing solution was consisted on 19.5 g of distilled water, 0.05 g of QDs and 0.5 g of gelatin. The gelatin was added to restrict the aggregation of QDs.

The nonlinear refraction and nonlinear absorption were observed in this water solution of QDs at the wavelength of 1064 nm (Fig. 3a). In the case of CA Z-scan the positive sign of γ was observed. The γ and β were determined using the standard fitting procedure of Z-scans. The nonlinear refractive index and nonlinear absorption coefficient of this solution at λ = 1064 nm were found to be 5.5×10^{-16} cm^2 W^{-1} and 3.2×10^{-11} cm W^{-1}, respectively. The γ and β of QDs were calculated to be 2×10^{-13} cm^2 W^{-1} and 1.2×10^{-8} cm W^{-1} taking into account their volume part in this solution (2.7×10^{-3}). The application of different intensities of 1064 nm pulses did not lead to the change of β, which points out the third-order process of 2PA as the main mechanism responsible for nonlinear absorption. The nonlinear absorption was also analyzed in the case of two energies (0.034 and 0.047 mJ) of 532 nm pulses (Fig. 3b). The minimal normalized transmittances in these cases were $T_{0.034\ \mathrm{mJ}} = 0.86$ and $T_{0.047\ \mathrm{mJ}} = 0.64$. The corresponding β of solution were found to be 1×10^{-10} and 1.5×10^{-10} cm W^{-1} at two different energies of laser pulses. This discrepancy in the measurements of nonlinear absorption using different probe pulses indicates the influence of additional nonlinear absorptive processes

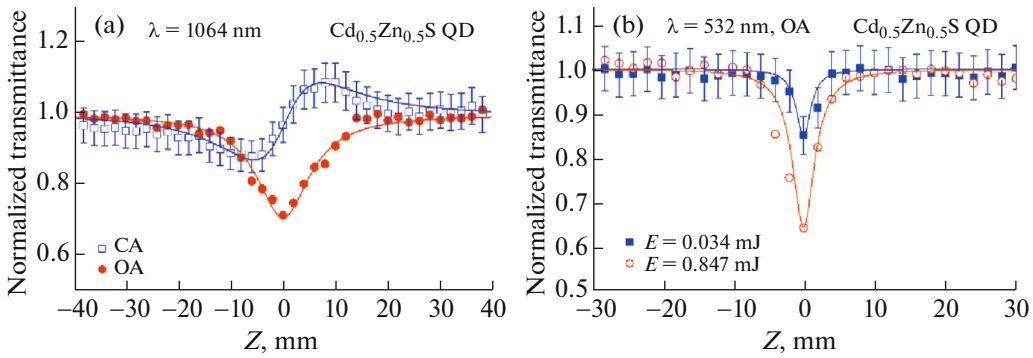

Fig. 3. Z-scans of $Cd_{0.5}Zn_{0.5}S$ QDs in water. (a) CA and OA Z-scans of $Cd_{0.5}Zn_{0.5}S$ quantum dots in water using 1064 nm radiation. CA: $E_{1064\ \mathrm{nm}} = 0.37$ mJ, OA: $E_{1064\ \mathrm{nm}} = 0.64$ mJ. (b) OA Z-scans of $Cd_{0.5}Zn_{0.5}S$ QDs in water using 532 nm pulses of different energy (0.034 and 0.047 mJ). Solid curves are the fittings to experimental data based on the standard relations of Z-scan theory. Reproduced from [28].

Table 1. Nonlinear optical parameters of pure QDs and QD + dye associates at the wavelengths of 1064 and 532 nm. The volume part of QDs in the solutions was taken into account for the calculations of γ and β. Reproduced from [28]

Sample	1064 nm		532 nm	
	γ, $cm^2\ W^{-1}$	β, $cm\ W^{-1}$	γ, $cm^2\ W^{-1}$	β, $cm\ W^{-1}$
Pure $Cd_{0.5}Zn_{0.5}S$ QDs	2×10^{-13}	$+1.2 \times 10^{-8}$	–	$+1.5 \times 10^{-7}$
$Cd_{0.5}Zn_{0.5}S$ + DEC	2.3×10^{-13}	$+1.4 \times 10^{-8}$	–	$+3 \times 10^{-7}$
$Cd_{0.5}Zn_{0.5}S$ + thionine	–	$+1.0 \times 10^{-8}$	–	$+2.3 \times 10^{-7}$
$Cd_{0.5}Zn_{0.5}S$ + erythrosine	–	–	–	-9×10^{-6}
		$+2.4 \times 10^{-8}$		$+1 \times 10^{-6}$

alongside with 2PA. Most expected mechanism of the variation of nonlinear absorption in that case is the involvement of RSA in overall decrease of propagation of stronger 532 nm pulses through the medium, rather than high-order NLO processes like three-photon absorption.

The influence of DEC on the values of γ and β of this dye-contained solution of QDs was almost insignificant compared with the γ and β measured in the water solution of QDs. Meanwhile, in the case of 532 nm the β of QD + dye associates was approximately two times larger than in the case of QD solution without dye. The values of nonlinear refraction indices and 2PA, SA, and RSA coefficients at the wavelengths of 1064 and 532 nm are collected in Table 1.

Similar results were obtained in the case of adding another dye (thionine) in water solution of $Cd_{0.5}Zn_{0.5}S$ QDs. In Fig. 4a, we analyze the dependence of normalized transmittance on the position of thionine-contained QD solution using OA Z-scan. The weak nonlinear absorption was observed at the wavelength of 1064 nm, while strong nonlinear absorption was obtained at the wavelength of 532 nm. The decrease of normalized transmittance of this solution at the valley was $\Delta T_{1064\ nm} = 0.21$ and $\Delta T_{532\ nm} = 0.36$, respectively, using 1064 nm (E = 0.63 mJ) and 532 nm (E = 0.028 mJ) pulses. β of this solution were calculated to be 1.0×10^{-11} cm W^{-1} (1064 nm) and 2.3×10^{-10} cm W^{-1} (532 nm).

The nonlinear absorption and SA in the $Cd_{0.5}Zn_{0.5}S$ QD + erythrosine associates was also analyzed at 1064 and 532 nm radiation. In Fig. 4b, OA Z-scans demonstrating different types of nonlinear absorption in this solution are presented. The absorption spectra of this solution show strong linear absorption band centered at the wavelength of 520 nm (Fig. 1). In this sample, the nonlinear refraction was not observed at both used wavelengths. Meanwhile, it demonstrated strong 2PA, SA, and RSA. The 2PA was the main mechanism of nonlinear absorption at the fundamental wavelength of Nd:YAG laser (empty squares). At the same time, SA and RSA were dominated at the wavelength of second harmonic of laser radiation at different energies of focused beam (empty circles and filled circles). Standard OA Z-scan fitting allowed determining the sign and magnitude of positive and negative nonlinear absorption coefficients of this solution, as well as saturation intensity (I_{sat}) of SA.

One can see that SA, which dominates over RSA at relatively small energies of 532 nm pulses (E =

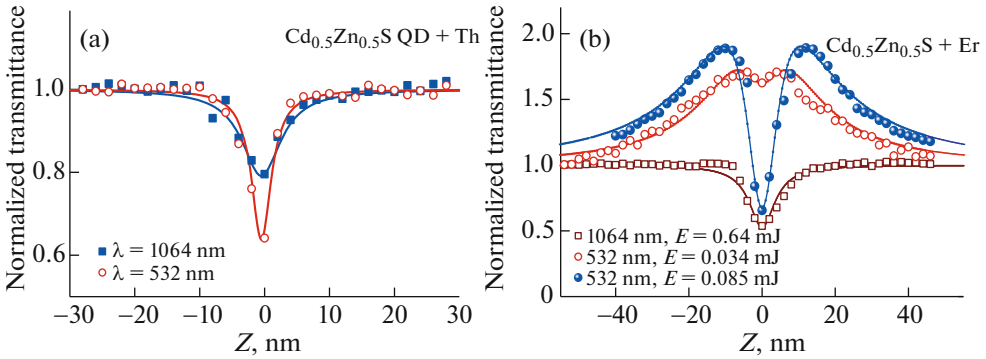

Fig. 4. (a) OA Z-scans of $Cd_{0.5}Zn_{0.5}S$ QD + thionine associates in water using 1064 nm (E = 0.63 mJ) and 532 nm (E = 0.028 mJ) pulses. Solid curves are fitted to the experimental data. (b) OA Z-scans of $Cd_{0.5}Zn_{0.5}S$ QD + erythrosine associates in water using 1064 nm (0.64 mJ) and 532 nm (0.034 and 0.085 mJ) pulses. Solid curves are fitted to the experimental data in accordance with the relations of Z-scan theory and phenomenological theory of SA. Reproduced from [28].

0.034 mJ, empty circles in Fig. 4b), becomes less pronounced at higher pulse energies ($E = 0.085$ mJ, filled circles) with regard to significantly stronger RSA effect. This difference in the involvement of SA and RSA is clearly seen in the area close to the focal plane of focusing lens (i.e., near $z = 0$ mm where laser radiation had largest intensity). Further growth of pulse energy led to appearance of deeper valley and larger decrease of normalized transmittance in the vicinity of $z = 0$ mm (down to $T \approx 0.45$). The intensity of laser pulses at these conditions was close to the one at which largest value of OL (~2.1) was achieved.

The nonlinear absorption processes at $\lambda = 532$ nm in the cases including SA and RSA were analyzed by the $\alpha(I) = \alpha_0/(1 + I/I_{sat}) + \beta I = \alpha_{SA} + \alpha_{RSA}$ relation for intensity-dependent absorption coefficient [31]. Here, α_0 is the linear absorption coefficient and I is the intensity of laser pulse. NLO coefficients were consisted on two parts: one related with saturable absorption (α_{SA}) and another related with reverse saturable absorption (α_{RSA}). Using this model the saturation intensity ($I_{sat} = 3 \times 10^{10}$ W cm^{-2}) for studied QD + dye associates was calculated. Meanwhile, the β of this solution associated with RSA was calculated to be 3×10^{-9} cm W^{-1} (at $\lambda = 532$ nm). One can estimate the β of QD + dye associates at these conditions to be ~1 $\times 10^{-6}$ cm W^{-1} taking into account the volume part of those species in the solution. This strong nonlinear absorption was responsible for OL of 532 nm radiation (Fig. 2).

QDs and dye molecules allow both resonance excitation of energetic levels and resonance transfer of energy. Most probably the observed effect of OL was caused by photosensibilization of these associates due to presence of the dyes possessing larger effective cross-section of the two-photon transition of QDs compared with the cross-section of photoionization. Additionally, the transfer of electrons from erythrosine onto the conduction zone has larger probability, due to small ionization potential, which increases the cross-section of the population of upper state, thus increasing the RSA of 532 nm picosecond radiation in the QD + dye associates.

3. NONLINEAR OPTICAL CHARACTERIZATION OF Ag_2S QUANTUM DOTS IN THE FIELDS OF PICOSECOND AND FEMTOSECOND UV AND IR PULSES

3.1. Peculiarities of Silver Sulfide QD Studies

With the advent of laser pulses in femtosecond time domain the need in materials which offer effective protection from lasers of certain wavelengths in different power regimes became significant. Among various materials semiconductor nanoparticles have excellent and interesting applications in optics and, particularly in optical limiting. For this reason, any new synthesized semiconductor nanoparticles or quantum dots (QDs) require to be examined under different conditions using laser pulses of variable energies, wavelengths and durations to understand NLO mechanisms and distinguish their attractive properties for practical applications. In many semiconductor nanoparticles the decrease of their sizes can provide a way to tune their physical properties and observe new phenomena [32, 33]. In particular, colloidal semiconductor nanocrystals provide strong size-related optical and optoelectronic properties. These properties have been investigated for applications in solar cells [34], light-emitting diodes [35], thin-film transistors [36], and biological imaging [37].

The QDs-containing materials, particularly sulfide-based QDs, were given special attention due to their large low-order optical nonlinearities [38, 39]. Particularly, various NLO processes can be induced in the ZnS nanoparticles which are useful in photonics [40]. The coexistence of RSA and 2PA in silver sulfide suggests that Ag_2S QDs could be a very promising nonlinear medium for photonic devices in different time scales if these semiconductor nanocrystallites are incorporated in appropriate media, which retain the attractive features of both components. The Ag_2S QDs also demonstrate low-threshold OL in the visible and near-IR ranges [41, 42]. With low power CW laser irradiation at 532 nm the large nonlinear refractive index up to -1.5×10^{-7} cm^2 W^{-1} in Ag_2S samples was reported [43]. The nonlinear absorption coefficients in the case of Ag_2S QDs dispersed in gelatin and thioglycolic acid were measured to be 7×10^{-11} and 8×10^{-11} cm W^{-1} using 532 nm pulses [44].

QDs may show variable NLO properties at different pulse durations and wavelengths. When QDs were pumped by nanosecond laser at 532 nm wavelength, most of measurements have shown RSA [45]. However, when nanoparticles are excited by pico- and femtosecond laser pulses at wavelengths of 800 and 1064 nm, they can exhibit self-focusing effects, as well as negative and positive nonlinear absorption [46–49]. Notice that in most of previous studies of silver sulfide nanoparticles the optical nonlinearities were analyzed at the wavelengths of 532 and 1064 nm. Meanwhile, there is a shortage of the studies devoted to the analysis of NLO properties of Ag_2S QDs at wavelengths of Ti:sapphire femtosecond and picosecond laser and its second harmonic (800 and 400 nm). Below we review NLO studies of Ag_2S QDs in the fields of picosecond and femtosecond UV and IR pulses [50].

3.2. Preparation and Characterization of Ag_2S Quantum Dots

The experimental procedure performed for the synthesis of silver sulfide quantum dots was adapted from the one described in [51]. QDs were twice cleaned by methyl alcohol in the centrifugal machine. To avoid the effect of too high concentration for the

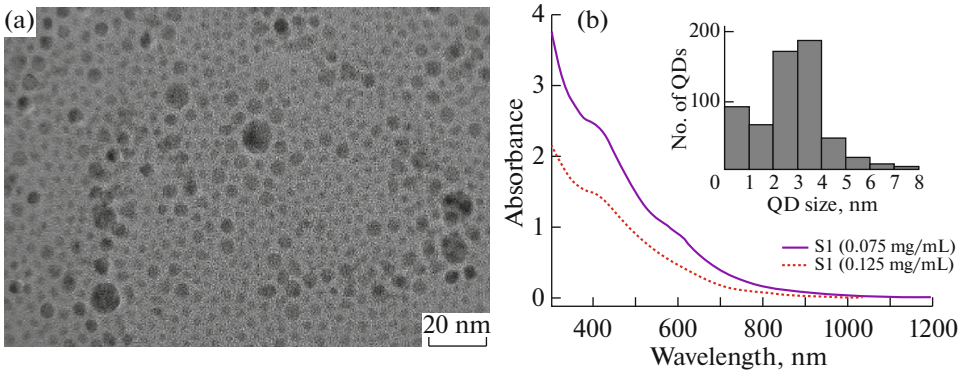

Fig. 5. (a) TEM image of Ag_2S QDs. (b) Absorption spectra of the S1 and S2 samples inserted in the 10 mm thick cells. Inset: histogram of Ag_2S QDs size distribution. Reproduced from [50] with permission of Springer.

linear absorption measurements the prepared QDs in water were diluted to make the samples containing different volume parts of QDs. Ag_2S QDs of higher (0.375 mg/mL) and lower (0.125 mg/mL) concentrations, which correspond to 1.5×10^{-3} and 5×10^{-4} mol/L concentrations, were synthesized and marked as S1 and S2, respectively.

The synthesized samples were characterized by TEM and absorption spectroscopy. TEM analysis provided information about size distribution (see inset in Fig. 5b) and morphology of the synthesized QDs (Fig. 5a). It is seen from Fig. 5b that QDs of different sizes with a narrow distribution are present in the synthesized samples. The calculated average size of the QDs was about 4 nm.

Figure 5b shows the absorption spectra of S1 and S2 samples. The absorption curves were similar to each other with the corresponding band gaps (E_g) of these two samples defined to be 3 eV ($\lambda \approx 410$ nm). These absorption spectra represented a superposition of absorption spectra of the QDs of different sizes. The small nanocrystals QDs (2–5 nm) showed a blue shift in the absorption edge that led to the change of effective band gap compared with the value ($E_g = 0.9$ eV) for bulk Ag_2S. The much larger band gap should cause a change of the refractive index and nonlinear absorption of this material. Notice also the presence of small band at ~600 nm in the case of S1 sample.

The standard Z-scan scheme is a convenient method to measure NLO parameters of materials. In reviewed studies, Ti:sapphire laser provided 60 fs, 800 nm and 200 ps, 800 nm pulses at 1 kHz pulse repetition rate. The second harmonic of this radiation ($\lambda = 400$ nm) was also used to analyze NLO properties in the vicinity of the SPR.

The noncollinear pump-probe technique was employed to analyze transient absorption (TA) in Ag_2S QDs using 400 nm radiation. The 800 nm radiation was split by a beam splitter at the ratio of 30:70. The transmitted beam was used as a pump pulse and the reflected beam was used as probe pulse. Prior to focusing to the sample, the probe pulse propagated through the delay line for the control of delay between the pump and probe pulses. Conversion of pump and probe pulses to 400 nm wavelength was accomplished using the 2-mm thick barium borate (BBO) crystals. Pump and probe pulses at $\lambda = 400$ nm of similar (vertical) polarization were focused using 300 mm focal length lens on the sample contained in the 2-mm thick fused silica cells. The pump power was 45 times higher than that of the probe beam. The zero delay between the pump and probe pulses was determined by using a 0.2-mm thick type-I BBO crystal at the focal point of two beams at the wavelength of 800 nm. Time delay between pump and probe pulses was controlled using the motorized translational stage with the single step of 7.4 μm. Ultrafast photodiode was used to measure the transmittance of the probe pulse at each position of translation stage. For the acquisition of TA profile the photodiode connected to the multi domain oscilloscope and the translational stage interfaced with motion controller were used.

3.3. Determination of NLO Characteristics of Ag_2S QD Suspensions

Attention was given to prevent optical breakdown of the samples. The intensities for breakdown of more dense Ag_2S suspension (S1) were measured to be 2×10^9 W cm^{-2} (for 200 ps, 400 nm pulses), 4×10^{10} W cm^{-2} (for 200 ps, 800 nm pulses), 6×10^{11} W cm^{-2} (for 60 fs, 400 nm pulses), and 8×10^{11} W cm^{-2} (for 60 fs, 800 nm pulses). Correspondingly, the maximal used intensities of probe pulses were 3×10^8 (for 200 ps, 400 nm pulses), 6×10^9 (for 200 ps, 800 nm pulses), 4×10^{11} (for 60 fs, 400 nm pulses), and 5×10^{11} W cm^{-2} (for 60 fs, 800 nm pulses). Prior to Z-scans of studies of Ag_2S suspensions, the components involved in suspensions formation (TOP, butanol, methyl alcohol, and water) were probed and

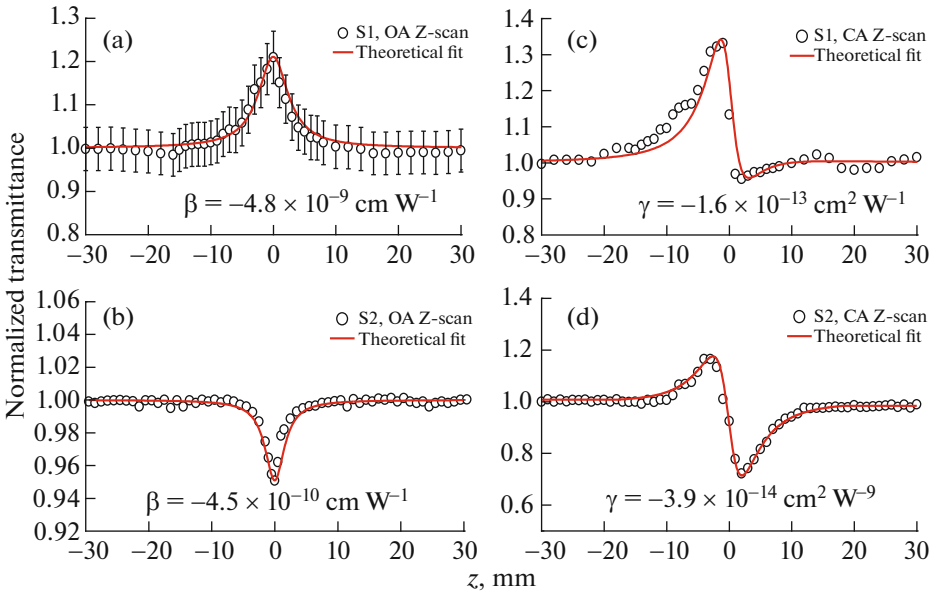

Fig. 6. OA and CA Z-scans of S1 and S2 measured using 200 ps, 800 nm probe pulses. Reproduced from [50]. With permission of Springer.

found that neither of them showed noticeable NLO response at given experimental conditions.

NLO characteristics of Ag_2S QDs were determined by analyzing OA and CA Z-scans. The experimental records are taken by moving the sample along z-axis from negative to positive position with respect to the focal plane. Initially, the samples S1 and S2 were analyzed using picosecond pulses (Fig. 6). S1 sample in the case of picosecond probe pulses (800 nm, 200 ps) showed SA (Fig. 6a). Notice that SA was observed only in the case of the high concentration of Ag_2S QDs. To fit OA Z-scan of S1 the standard equations of Z-scans were used from which I_{sat} of S1 and β were determined to be 2.8×10^{10} W cm^{-2} and -4.8×10^{-10} cm W^{-1}. The fit of OA Z-scan to the experimental data for S2 is depicted in Fig. 6b by the solid curve, and the nonlinear absorption coefficient was calculated to be 4.5×10^{-10} cm W^{-1}. It was found that at small fluence (F) of 800 nm, 200 ps pulses (F = 10 mJ cm^{-2}, $I_0 = 5 \times 10^7$ W cm^{-2}) SA was dominating at larger concentration of QDs. This process was transformed to RSA or, most probably, 2PA at larger fluence of probe pulses (F = 50 mJ cm^{-2}, $I_0 = 2.5 \times 10^8$ W cm^{-2}) and smaller concentration of QDs.

Similar equation was used for fitting the theoretical dependences and measured normalized transmittances of CA Z-scans taking into account the experimental conditions. The values of γ and β for two samples were consequently found after fitting of ρ and $\Delta\Phi_0$. The latter parameter was close to the measurements of positive and negative nonlinear absorption performed using OA Z-scan scheme (Figs. 6a, 6b).

Figures 6c, 6d show the results of CA measurements demonstrating the self-defocusing in S1 and S2 samples using 800 nm, 200 ps pulses. The fitting procedure of CA Z-scans (solid curves in Figs. 6c, 6d) allowed calculating γ of S1 and S2 to be -1.6×10^{-13} and -3.9×10^{-14} cm^2 W^{-1}, respectively.

In the case of shorter wavelength of the picosecond probe pulses (200 ps, 400 nm), a decrease in the normalized transmittance at focal area was observed for both samples. This process was probably related with RSA. The values of β in the case of 400 nm, 200 ps probe pulses were close to the earlier reported data measured using 532 nm nanosecond pulses (~5×10^{-8} cm W^{-1} [52]) for similar samples. CA measurements using 400 nm, 200 ps pulses showed self-defocusing of two samples along the whole range of probe pulse energies. γ's of these two samples were nearly similar to each other [-6×10^{-13} and -5×10^{-13} cm^2 W^{-1}].

Meanwhile, the results obtained during OA and CA Z-scans of S1 and S2 using IR femtosecond probe pulses (800 nm, 60 fs; Figs. 7c and 6d) were different compared to the previous case. CA Z-scan curves showed the self-focusing, when valley was followed by the peak, contrary to the case of 400 nm, 200 ps probe pulses. The approximately similar values of γ were measured in that case (3×10^{-16} and 2.3×10^{-16} cm^2 W^{-1}). Notice that CA Z-scans using UV femtosecond pulses (400 nm, 60 fs) showed self-defocusing in sample S2, similarly to the case of 400 nm, 200 ps pulses.

SA and RSA do not play important role in Ag_2S QDs in the case of 800 nm, 60 fs pulses. For direct transition of Ag_2S QDs the excitation energy (1.55 eV)

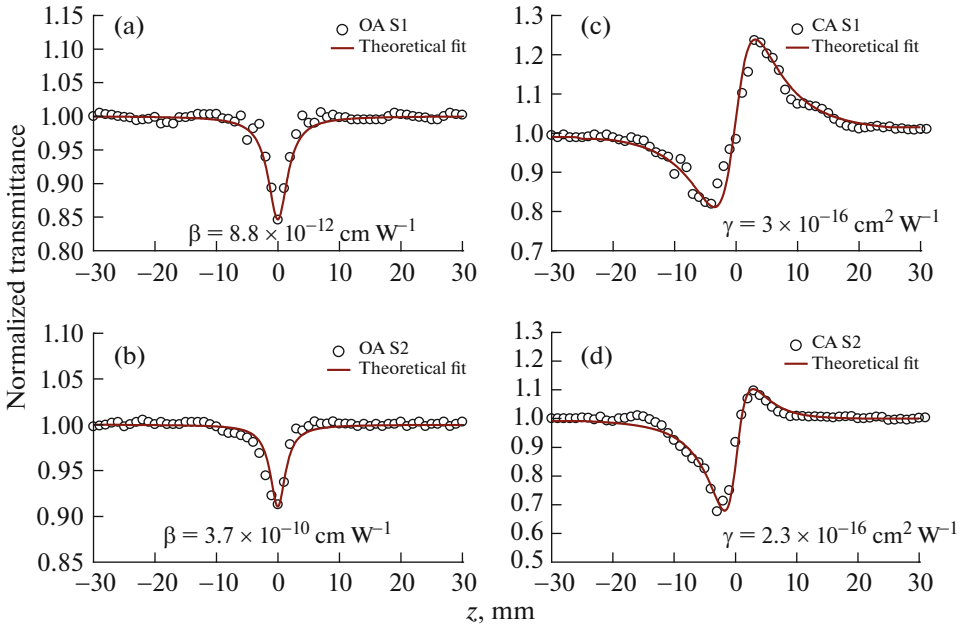

Fig. 7. OA and CA Z-scans of S1 and S2 using 60 fs, 800 nm pulses. Reproduced from [50]. With permission of Springer.

is lower than the band gap energy of Ag_2S QDs (3 eV), and, hence, the interband transition is allowed by 2PA at the laser wavelength of 800 nm. The OA Z-scans at two concentrations of Ag_2S QDs showed 2PA (Figs. 7a, 7b). The 3-fold difference in concentration of these two samples led to the decrease of the nonlinear absorption coefficient from 8.8×10^{-12} to 3.7×10^{-12} cm W^{-1}. In the case of 400 nm, 60 fs pulses, the most probable nonlinear absorption mechanism was RSA. NLO parameters of Ag_2S QD suspensions measured using 1 kHz pulses are collected in Table 2.

Table 2. Nonlinear optical parameters of Ag_2S QD suspensions calculated at different experimental conditions. Reproduced from [50]. With permission of Springer

QD	I_0, W cm^{-2}	I_{sat}, W cm^{-2}	γ, cm^2 W^{-1}	β, cm W^{-1}
Measurements using 200 ps, 800 nm radiation				
S1	3.4×10^8	2.8×10^{10}	-1.6×10^{-13}	-4.8×10^{-9}
S2	1.8×10^9		-3.9×10^{-14}	4.5×10^{-10}
Measurements using 200 ps, 400 nm radiation				
S1	8.9×10^7		-5.6×10^{-13}	9.8×10^{-8}
S2	8.9×10^7		-5×10^{-13}	4.8×10^{-8}
Measurements using 60 fs, 800 nm radiation				
S1	2.2×10^{11}		3×10^{-16}	8.8×10^{-12}
S2	2.7×10^{11}		2.3×10^{-16}	3.7×10^{-12}
Measurements using 60 fs, 400 nm radiation				
S2	1×10^{11}		-2×10^{-15}	5×10^{-11}

3.4. Pump-probe and Optical Limiting Studies

TA in Ag_2S QDs immersed in toluene was studied using 400 nm, 60 fs pulses. Pump pulse fluence of 20 mJ cm^{-2} ($I_0 = 3 \times 10^{11}$ W cm^{-2}) and probe pulse fluence of 0.45 mJ cm^{-2} ($I_0 = 7 \times 10^9$ W cm^{-2}) were used in the discussed studies, which fulfill the criteria for TA measurements. In Fig. 8a, the temporal evolution of TA is shown. TA measurement was also performed for pure toluene to eliminate its influence on TA profile of Ag_2S QDs. TA profile was fitted with double exponential profile to obtain the decay time constants associated with relaxation of excited phonons at 400 nm irradiation. The characteristic time constants were determined to be 1.7 and 6.9 ps that can be attributed to the electron–phonon and phonon–phonon interactions in Ag_2S QDs.

Notice that there are no reports about the dynamics of the excitation of these quantum dots at resonance conditions. The determined time constants are consistent with the earlier reported data [53, 54] where TA studies were performed for the case of Ag_2S QDs in ethylene glycol in the near-IR region. The relaxation dynamics, which can become faster as the pump pulse energy increases, was attributed to Auger recombination process. However, in these experiments SPR at ~400 nm corresponded to the quasi-resonant conditions for Ag_2S QDs irradiated by 400 nm pulses. This can probably lead to saturation of absorbance followed with the increase in the transmittance of probe pulses at higher intensity of pump radiation at the employed concentration (S1) of Ag_2S QDs in toluene.

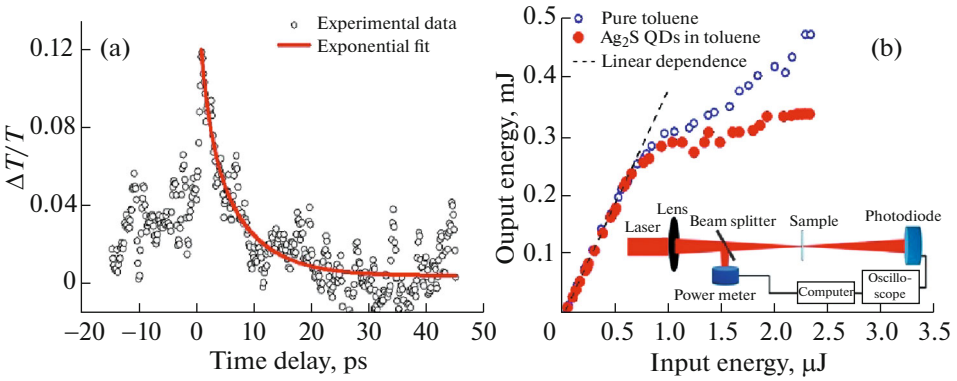

Fig. 8. (a) Transient absorption of As_2S QDs excited at 400 nm. (b) Optical limiting of 800 nm, 60 fs pulses in pure toluene (empty circles) and Ag_2S QD suspension in toluene (filled circles). Inset: Setup for OL studies. Reproduced from [50]. With permission of Springer.

OL was demonstrated using the 800 nm, 60 fs pulses propagating through Ag_2S QD suspension in toluene. This effect was attributed to 2PA. The suspension was placed close to the focal plane of 400 mm focal length lens (see inset in Fig. 8b). The energy of 800 nm pulses was gradually increased and measured before and after propagation through the 2-mm-thick cell containing QD suspension S2 (Fig. 8b, filled circles). The linear dependence between input and output pulses was maintained up to the input pulse energy of ~0.7 μJ. The transmittance of QD-containing cell decreased with further growth of pulse energy. This decrease of transmittance with the growth of laser intensity was also observed in OA Z-scan measurements using 800 nm, 60 fs pulses (Figs. 7a, 7b). Further increase of input pulse energy led to OL of the energy of propagated laser radiation. OL was also observed in the case of pure toluene starting from approximately the same energy (0.8 μJ; Fig. 8b, empty circles). These two curves show that QDs enhance OL of this suspension even compared to the liquid (toluene) possessing large nonlinear absorption.

3.5. Analysis of the Optical Nonlinerities of Studied QDs

Previously, analysis of the sign variations of γ was performed in the case of semiconductors [55]. The used Kramers–Kronig model provided some clues in definition of γ's sign transformation from self-focusing to self-defocusing and vice versa once one uses different wavelengths of probe pulses. The crucial parameter in their model is the band gap value of semiconductor. Meanwhile, once the sizes of semiconductor decrease below ~5 to 10 nm their band gap drastically increases. It is not clear whether it is correct to consider Ag_2S QDs as semiconductors. Below we address the modification of the sign of nonlinear refractive index using the Kramers–Kronig relations for QDs.

An important characteristic of metal sulfide QDs is the band gap controllable by the size effect. This peculiarity of QDs can strongly change their NLO properties, in particular the sign of nonlinear refraction. The analysis of nonlinear refraction of S1 and S2 showed that they demonstrate self-focusing properties (Figs. 7c, 7d) once femtosecond 800 nm pulses were used as the probe radiation. The nonlinear Kramers–Kronig relations predict the self-focusing in semiconductors for which the relation $\hbar\omega/E_g < 0.69$ takes place [55]. Here, $\hbar$ is the Planck's constant, ω is the frequency of laser radiation, and E_g is the bandgap energy of semiconductor (3 eV in the case of Ag_2S QDs). The corresponding $\hbar\omega/E_g$ value for suspensions at λ = 800 nm was calculated to be 0.53. Thus, one can expect a positive sign of γ in these two suspensions (S1 and S2) that was confirmed in our experiments. Correspondingly, the experiments with 400 nm, 60 fs probe pulses showed the self-defocusing properties of our samples that corroborates with above consideration ($\hbar\omega/E_g$ = 1.06). The reason of relatively small values of nonlinear refractive indices of Ag_2S QD suspensions at 800 nm (3×10^{-16} cm^2 W^{-1}) can be related with the proximity of their $\hbar\omega/E_g$ values to 0.69 (i.e., at $\lambda \approx 620$ nm) where the sign of γ changed from positive to negative. Far from this wavelength (i.e., at 400 nm) the nonlinear refractive index showed notably larger value (2×10^{-15} cm^2 W^{-1}).

Meanwhile, the use of longer probe pulses demonstrated the self-defocusing properties of the studied samples in the case of both 400 and 800 nm radiation. Below we analyze the change of sign of nonlinear refraction in the case of longer pulses. There are some fast processes (intermolecular interaction, molecular reorientational Kerr effect, electronic Kerr effect) that can originate from NLO response of Ag_2S particles and contribute to the overall nonlinear adding of the refractive index. The slowest among them is the process connected with the reorientation of molecules. Previously, the relaxation times of these three processes were reported as ~1.5 ps for reorientation of

molecules [56] and ~200 fs for other processes [57]. The former process can either increase the effective nonlinear refractive index (in the case of positive value of reorientational processes) or decrease or even change the sign of this parameter in the case of relatively long pulses. The reviewed results indicating the change of the sign of γ at a probe pulse duration (200 ps) compared to the 60 fs pulses confirm the assumption of the negative addition of some nonlinearities (intermolecular interaction and molecular reorientational Kerr effect) to the purely electronic Kerr effect attributed to the influence of ultrafast pulses. In other words, the growth of pulse duration above the femtosecond range can lead to involvement of the above mentioned slow processes, which overpass the purely electronic Kerr effect in our samples. The negative value of the former processes causes the change of sigh of the effective nonlinear refractive index of suspension.

Notice that actual values of the nonlinear susceptibilities of QDs are considerably higher than those of QD suspensions due to small fraction of particles in the whole volume of solvent. A simplest method for the estimation of the nonlinear susceptibilities of such particles is to divide the nonlinear susceptibility of compound by the volume or weight part of QDs. More precisely, the third-order nonlinear susceptibilities ($\chi^{(3)}$) of composites, and, correspondingly, γ and β, are also enhanced by the local field factor as

$$\chi^{(3)} = p|f|^2 f^2 \chi^{(3)}_{QD}, \quad (1)$$

where $\chi^{(3)}_{QD}$ is the third-order nonlinear susceptibility of QDs, f is the local field factor, which in the case of Ag_2S QDs was analyzed in [58, 59], and p is the volume fraction of nanoparticles or QDs. The square of the local field factor for the semiconductor QDs embedded in many dielectric materials is often of the order of 0.2–0.4 [58].

NLO parameters shown in Table 2 are attributed to the suspensions of Ag_2S QDs. The estimates show that the volume fraction of QDs in suspensions was in the range of 10^{-3}. In particular, β of S1 suspension at 400 nm, 200 ps probe pulses was measured to be ~10^{-7} cm W^{-1}. One can estimate β of QDs at these conditions to be ~1×10^{-3} cm W^{-1} taking into account the volume fraction of small-sized species in the solution and local field factor ($|f|^2 \sim 0.3$). Similarly, each value of γ and β of suspensions presented in Table 2 should be divided by a factor of $p|f|^2 f^2 \approx 10^{-4}$ to determine these parameters attributed to Ag_2S QDs.

In these studies, the aqueous suspensions of Ag_2S quantum dots were used. To explain the increase in NLO response of this suspension, the local field factor should be considered. Meanwhile, the medium in which the studies were conducted is a composite material. Therefore, it is worth additionally analyzing it as an "effective" medium consisting of two components possessing different nonlinearities.

Actually, the suspensions consisted on the water and QDs, while the concentration of some other residual components participated in the synthesis of quantum dots was notably smaller with regard to the two main species. NLO response of water was checked at used experimental conditions. Neither fast (i.e., Kerr-related) NLO properties nor slow thermal accumulation-induced effects were observed in water at the maximal used intensities and energies of 200 ps and 60 fs pulses. Particularly, the discussed studies showed the insignificant role of thermal-induced variations of the refractive indices of suspensions at 1 kHz pulse repetition rate. Thus the surrounding medium did not play role of thermal lens or Kerr medium along the whole set of these studies. From this one can conclude that NLO processes observed during these studies can be attributed solely to the presence of Ag_2S QDs in the suspensions.

Those measurements allowed determining the relative role of nonlinear absorption and nonlinear refraction in Ag_2S QDs. The Stegeman figure of merit $T = |2\beta\lambda/\gamma|$ shows the prevailing influence of nonlinear absorptive properties of used QDs over their nonlinear refraction ($T = 5$ and $T = 4.8$ in case of picosecond and femtosecond pulses at both 800 and 400 nm, respectively).

Below we briefly address the usefulness of analysis and variations of NLO parameters in small-sized QDs with respect to larger-sized nanoparticles. QDs with sizes less than 4 nm can play a predominant role in the overall nonlinear refractive index of such structures due to the quantum confinement effect. The positive sign of γ attributed to small QDs can prevail with respect to the negative sign of γ in the case of larger-sized nanoparticles when electronic Kerr effect plays dominating role in NLO variations of refractive index. This peculiarity can lead to the difference in NLO properties of bulk materials, large-sized nanoparticles, and small-sized QDs. Moreover, as reviewed studies show, pulse duration is another dominating factor for determination of the sigh of γ of these species.

4. EFFICIENT HIGH-ORDER HARMONIC EMISSION FROM METAL SULFIDE QUANTUM DOTS

4.1. Perspectives in Application of Low-dimensional Aggregates for Harmonic Generation

Previous studies on HHG after ablation of nanoparticle-containing targets have revealed the advantages of such species for frequency conversion in the XUV range [60, 61]. A larger cross-section of recombination and the possibility of recombination of an accelerated electron with the parent particle through either recombination with the same or a neighboring atom, or with the multi-atomic particle as

a whole, were considered as the most probable reasons for the growth of HHG yield in such plasmas. In these earlier studies, the experimental conditions were not optimized, in particular, the delay between the heating and driving pulses. Nevertheless, even at those non-optimal conditions, the harmonic yield was already higher than in the case of ablation of bulk targets of the same material [62]. Since in these studies short delays of up to 100 ns between the heating and driving pulses were employed, it was not clear how nanoparticle species could influence the processes of frequency conversion, because there were no proofs of their presence in the interaction region with the driving laser. One explanation was based on the disintegration of larger species into small clusters and monoatomic species, which probably could reach the interaction area at the short delays employed. However, no sufficient confirmation of this assumption has been provided. Taking into account the anticipated velocities of atoms, molecules and ions ($\sim 1 \times 10^4$ m s^{-1}), QDs ($\sim 1 \times 10^3$ m s^{-1}) and nanoparticles [$(1-5) \times 10^1$ m s^{-1}] of the same material one can expect their arrival in the region of the femtosecond laser beam propagation a few tens of nanosecond, a few hundreds of nanosecond, and a few tens of microsecond from the beginning of ablation, respectively.

To match the propagation of the driving pulse and the highest concentration of the studied group of multi-atomic species one, therefore, has to use the electronic delay between the heating and the driving pulses. The application of two electronically separated pulses from different lasers synchronized by a digital delay generator allows analyzing the involvement of various species in such multi-particle plasmas in HHG process. Application of this approach for HHG in multi-particle plasmas, alongside with other methods of harmonic enhancement, requires the analysis of the ablated species to temporally match them with the propagation of driving femtosecond pulses through the plasma.

QD-containing materials, particularly metal sulfide based QDs, have attracted special attention due to their large low-order optical nonlinearities [63, 64]. Various NLO processes can be induced in the ZnS nanoparticles, which became useful in photonics [65]. The coexistence of reverse saturable absorption and two-photon absorption in silver sulfide suggests that Ag_2S QDs could be a very promising nonlinear medium for photonic devices in different time scales if these semiconductor nanocrystallites are incorporated into appropriate media while retaining the attractive features of both components. Ag_2S QDs also demonstrate low-threshold OL in the visible and near-IR ranges [66]. Meanwhile, there are so far no studies devoted to the analysis of the high-order NLO properties of metal sulfide QDs were reported. Below we discuss the HHG in metal sulfide QDs [67].

4.2. Preparation of QD-containing Targets for HHG Studies

For improving the efficiency of HHG in a plasma containing QDs requires solving two problems: (1) developing the methods for the synthesis of metal sulfides QDs, followed by the formation of solid-state materials containing large concentrations of these species, and ensuring the stability of the morphology of vaporized materials under laser ablation, and (2) optimizing the process of converting the wavelength of laser pulses during HHG in a laser plasma containing such multi-particles.

The synthesis of QDs was carried out taking into account a number of criteria for their use to generate harmonics of ultrashort pulses. The first criterion is the formation (as a result of ablation of samples by either picosecond or nanosecond heating pulses) of a plasma cloud consisting of QDs, as well as atoms, ions, and clusters at the time of the passage of the converting femtosecond pulses above the target surface. The second criterion is the presence of the maximal concentration of QDs at the time of transmission of the femtosecond pulses through the plasma. The third criterion is the size characteristics of quantum dots. Previous studies of harmonic generation in multi-particle containing plasmas, as well as qualitative assessments, show that the most optimal sizes of such species should be in the range of 1–4 nm.

Synthesis of colloidal QDs of ZnS and CdS was carried out by mixing $CdBr_2 \cdot 4H_2O$, $ZnBr_2 \cdot 4H_2O$, and thioglucolic acid (TGA) in the required proportions. The corresponding salts of cadmium and zinc bromide were dissolved in water (200 mL) and then TGA was added. Then the 50 mL of Na_2S aqueous solution (1.3 mM) was injected into the prepared solution. The synthesized colloidal solution of QDs was dissolved by adding ethanol to a 50% solution, centrifuged and re-dissolved in water. The cleaning procedure was repeated several times. A similar procedure was used for the synthesis of Ag_2S QDs.

The synthesized samples of colloidal solutions of zinc, cadmium and silver sulfides were further used to produce the solid targets for laser ablation and generation of harmonics. A new method of increasing the filling factor Ag_2S, ZnS, and CdS QDs in the stabilizing polymer was developed to form solid samples of multi-particle species for laser ablation in vacuum and formation of the plasma torches containing a large amount of QDs required for efficient generation of harmonics. The method is based on the compatibility of synthesized colloidal QDs and gelatin, as well as the possibility of increasing the concentration of QDs during centrifugation in the presence of acetone. Gelatin's property of high filling ability as a polymer and the possibility of drying such samples to a solid state are among the advantages of this method. The preparation of solid tablets was accomplished in the following sequence: the prepared concentrated solution of

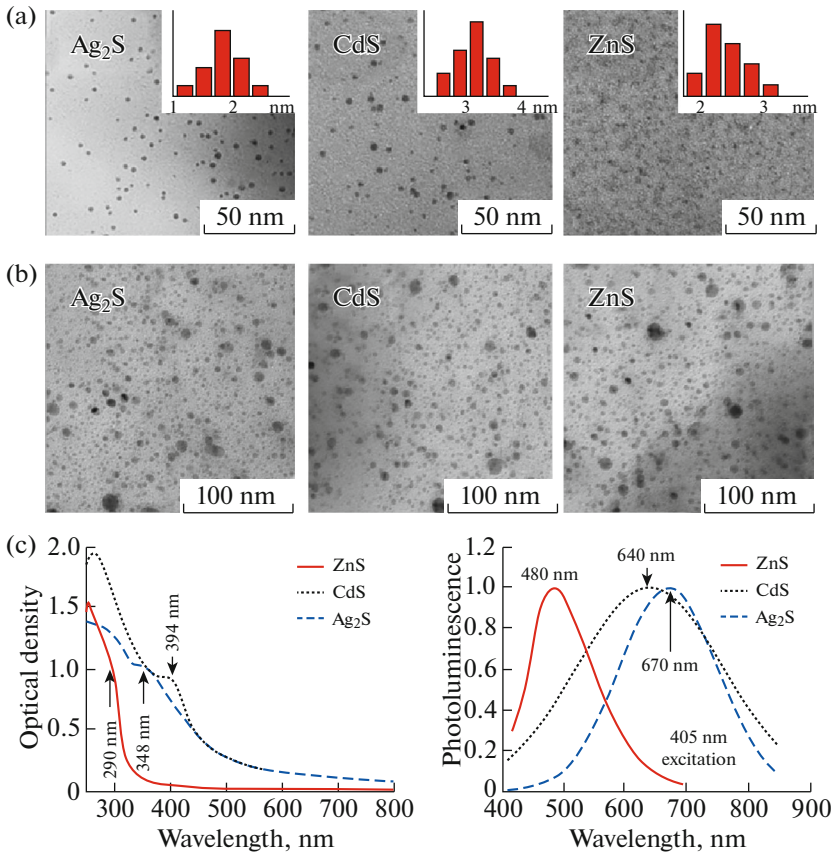

Fig. 9. (a) TEM images of synthesized metal sulfide QDs. (b) TEM images of Ag_2S, CdS, and ZnS QDs ablated at the 10 mJ energy of heating nanosecond pulse and deposited on nearby glass and silicon substrates. (c) Spectra of (left graph) optical absorption and (right graph) photoluminescence of synthesized QD. Reproduced from [67].

QDs was introduced into the gelatin melted at a temperature of 40–50°C using intensive stirring and then the suspensions were dried at a temperature of 80°C for 24 hours to a solid state and then placed for further vacuum drying where they were kept for 10 days. Control of the obtained samples was carried out by analysis of their luminescence, which was compared with the luminescence of the same QDs in TGA.

TEM images of synthesized metal sulfide QDs are shown in Fig. 9a. The size distribution is shown in the inset as histograms. From the histograms, one can conclude that Ag_2S QDs show mean sizes in the range of 1.7 to 2.0 nm, CdS QDs about 3.0 to 3.2 nm, and ZnS QDs about 2 to 2.2 nm diameter. The morphological studies reveal that Ag_2S QDs condensate in a monoclinic lattice, while CdS and ZnS QDs condensate in a cubic lattice and Ag_2S QDs in a monoclinic lattice. Figure 9b presents images of QDs ablated by 10 mJ and 5 ns pulses and deposited on nearby substrates. The collected particles confirm the presence of metal sulfide QDs within the plasma plume. The sizes of deposited particles were larger than those of original ones. Optical absorption and photoluminescence spectra are shown in Fig. 9c. The spectra were significantly blue shifted with regard to the bulk materials of similar materials. CdS, ZnS, and Ag_2S QDs were embedded in gelatin with about 20% weight and prepared in the form of 5 × 5 × 3 mm plates.

Synchronization of two laser sources, such as most commonly used Ti: sapphire femtosecond laser and Nd:YAG nanosecond laser, may resolve, to some extent, the puzzle related with the observation of the enhancement of the harmonics generating in the plasmas produced during ablation of multi-particle media. The main advantage of this approach is a possibility to electronically drive the delay between heating nanosecond and driving femtosecond pulses in a broad range. Additionally, the use of radiation from the nanosecond Nd:YAG lasers offers advantages in plasma formation compared with previously used picosecond pulses. The application of nanosecond pulses to ablate the targets allows the formation of less ionized and less excited plasma during a longer period of laser-matter interaction compared with the picosecond pulses. Nd:YAG lasers commonly operate at 10 Hz pulse repetition rate, which is more suitable for stable HHG in plasmas compared with 1 kHz ablation, though in the latter case some strategies, such as

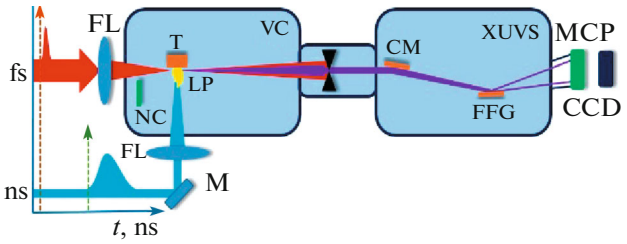

Fig. 10. High-order harmonic generation setup. FL, focusing lenses; fs, converting femtosecond pulses, ns, heating nanosecond pulses; VC, vacuum chamber; T, target; NC, BBO crystal; LP, laser plasma; XUVS, extreme ultraviolet spectrometer; CM, cylindrical gold-coated mirror; FFG, flat field grating; MCP, microchannel plate; CCD, CCD camera. Reproduced from [67].

target rotation [68], allowed, to some extent, improvement of the stability of 1 kHz coherent short-wavelength sources.

The metal sulfide QD plasmas were used for HHG. The driving femtosecond pulses (800 nm, 1 kHz; Spitfire Ace, Spectra Physics) propagated through the plasma at different delays from the beginning of target irradiation by nanosecond heating pulses (1064 nm, 10 Hz; Q-Smart, Coherent). The variable delay (0–10^6 ns) between 5 ns heating pulses and 30 fs driving pulses was established to generate harmonics in plasma at the used geometry of experiments when the 800 nm femtosecond pulses were focused onto the plasma area from the orthogonal direction with regard to ablating radiation, at a distance of ~200 μm above the target surface (Fig. 10). Additionally, the harmonic yield was maximized by adjusting the position of the target with regard to the optical axis of propagation of the driving femtosecond pulses and by varying the focusing position of this radiation with regard to the plasma. The harmonic emission was directed to XUV spectrometer containing a cylindrical mirror and a 1200 grooves/mm flat field grating with variable line spacing. The XUV spectrum was recorded by a microchannel plate (MCP) with a phosphor screen, and the harmonics were imaged by a CCD camera.

HHG was also carried out using the two-color pump (TCP) of plasma. The reason for using the TCP instead of the single-color pump (SCP) was related with earlier demonstrated advantages of this approach in the generation of odd and even harmonics in gases and plasmas [69–72], as well as larger efficiency of harmonic yield in the former case. TCP using 800 nm radiation as the first field and 400 nm radiation as the second field was applied to carry out the comparative analysis of TCP and SCP schemes. The 0.4-mm-thick BBO crystal (type I) was installed inside the vacuum chamber on the path of the 800 nm radiation to generate second harmonic (H2). The conversion efficiency of H2 pulses (λ = 400 nm) was relatively low (~4%). However, due to small group velocity dispersion in the thin BBO crystal, the overlap of these two pulses in plasma area was sufficient to determine how the weak second orthogonally polarized field influences the whole process of HHG in QDs.

4.3. Harmonic Generation

Figure 11 shows high-order harmonics generated from these QDs in the spectral range of 20–120 nm. HHG at different delays between the heating and driving pulses from 100 to 2000 ns is shown for pulse energies of 4 and 0.4 mJ, respectively. At initial stages of plasma formation and spreading out from the target, i.e., at delays less than 50 ns, the concentration of particles (neutrals and singly charged ions) was insufficient for HHG, since the whole ensemble of particles possessing velocities of ~2×10^4 m s^{-1} cannot reach the spatial region of the driving beam. At larger delays (above 100 ns) sufficient amounts of QDs appeared in the path of the femtosecond beam which allowed the generation of harmonics.

The optimal delay was different for three QD plasmas studied. At about 400, 300, and 250 ns the highest harmonic yield was observed for Ag_2S QD (atomic weight 247.8 amu), CdS QD (144.5 amu), and ZnS QD (97.5 amu), respectively. Notice that the use of a carbon plasma (atomic weight 12 amu) yielded maximal harmonic intensity at a significantly smaller delay of 30 ns between the heating and driving pulses using similar pulse energies. It should also be mentioned that harmonics generated from pure gelatin were almost one order of magnitude lower than those observed from QDs. The harmonic cut-off is higher for lighter QD species, e.g., at the 31st harmonic for ZnS while Ag_2S showed the 25th as highest harmonic. A further increase of the delay for each of these plasmas led to a gradual decrease of HHG efficiency. The harmonics almost disappeared once the delay exceeded 2 to 3 μs. No harmonics were observed at delays up to 50 μs.

Experiments using bulk targets of the same materials led to similar dependencies of the harmonic yield on the delay between the heating and driving pulses. These experiments showed that independently of whether molecules or QDs spread out from the target surface of the same material they appear in the area of the femtosecond beam approximately at the same time. Figure 12a shows the harmonic generation in the laser-produced plasma after ablation of bulk ZnS by 4 mJ pulses. The harmonic yield maximizes at about 200–500 ns delay.

Figure 12b shows a comparison of the harmonic yield in the case of ablation of bulk and QD-containing ZnS targets. It is obvious that QD plasma yield significantly stronger harmonics which also extend to higher orders. In the case of QD-containing plasma, the harmonics extended to ~50 eV (25 nm) or 31st order, while for the plasma produced from bulk

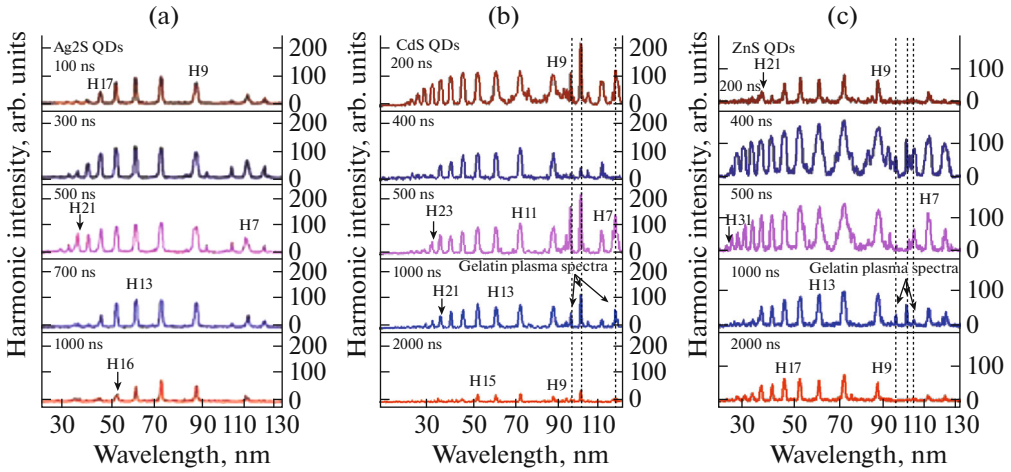

Fig. 11. Harmonic spectra from QD-containing plasmas [(a) silver sulfide QDs, (b) cadmium sulfide QDs, (c) zinc sulfide QDs] at different delays between heating and driving pulses. Dash-dotted lines show the plasma elision attributed to overexcited gelatin. Reproduced from [67].

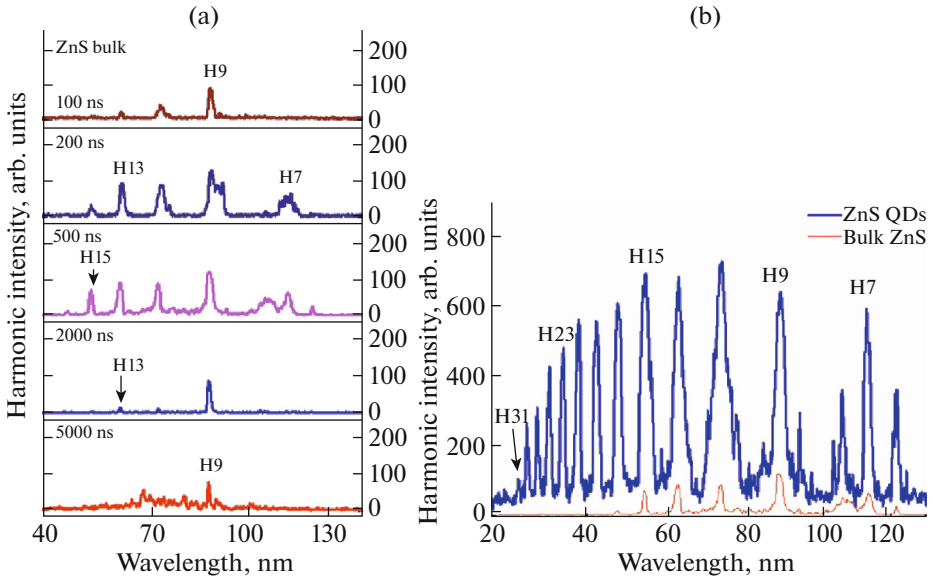

Fig. 12. (a) Harmonic spectra from the plasmas produced on the bulk ZnS surface at different delays between heating and driving pulses. The bottom panel was obtained at stronger excitation of the target (10 mJ). One can see the plasma emission lines from bulk zinc sulfide. (b) Comparison of harmonic distribution and intensities in the case of ablation of QD (thick curve) and bulk (thin curve) ZnS targets at 500 ns delay between the heating and driving pulses. The weight part of QDs in gelatin (20%) is taken in to account for comparison of HHG at similar concentrations of plasmas. Reproduced from [67].

ZnS the highest generated harmonic order was the 16th corresponding to a photon energy of ~26 eV (47 nm). The weight concentration of ZnS QDs in gelatin (0.2) was taken into account to carry out the comparison of HHG spectra produced from monoparticles and multi-particle plasma. The overall ratio of intensities of the lower-order harmonics generated in these two plasmas was ~7.

Figure 13 shows the plasma emission spectra of Ag_2S, CdS, and ZnS QDs in gelatin (three upper panels) and pure gelatin (bottom panel) using a larger energy of heating pulses (15 mJ). The majority of lines belong to gelatin emission, except the shorter-wavelength part of this spectrum. Most of the lines can be assigned to the emission from ionized carbon, as expected for gelatin. Those in the range of 45–90 nm seem mostly associated with C II emission. Probably, the existence of singly charged carbon caused the harmonic generation in pure gelatin plasma. These spectra underline that the metal sulfides were weakly

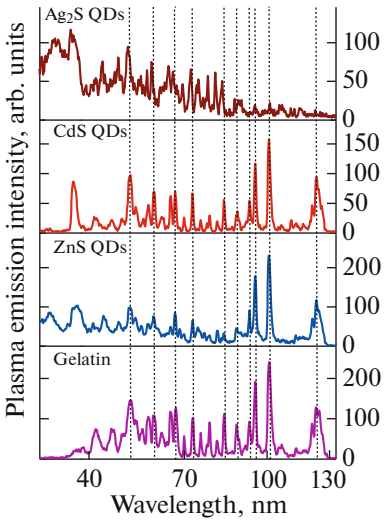

Fig. 13. Plasma emission spectra of Ag_2S, CdS, and ZnS QDs in gelatin (three upper panels) and pure gelatin (bottom panel). Dash-dotted lines show similar emission in all four plasmas. Reproduced from [67].

excited and ionized during ablation. This condition of "mild" ablation, when the existing density of free electrons in the plasma do not prevent the formation of phase matching conditions between the waves of the driving and harmonic fields, is a prerequisite for efficient HHG. Notice that the conditions of ablation, when the plasma emission shown in Fig. 13 dominates in XUV spectra, are unsuitable for efficient HHG due to the presence of a large number of free electrons which prevent an optimal phase relation between the driving and harmonic waves.

Lesser excitation of the QD containing targets (4 mJ) allowed the formation of plasmas suitable for harmonic generation. Odd harmonics of 800 nm radiation up to H25, H29, and H31 were achieved using Ag_2S, CdS, and ZnS QD plasmas, respectively (see Fig. 11). The appearance of strong harmonic emission did not coincide with the plasma emission from highly charged particles in the studied spectral range (20–120 nm), which confirms that these experiments were carried out at a soft ablation regime of QD containing targets. The driving pulse ($I \approx (2–5) \times 10^{14}$ W cm^{-2}) also did not cause the appearance of strong ionic emission from higher charged molecules and QDs.

A final set of HHG studies was performed using two orthogonally polarized driving pulses. A 0.4 mm thick BBO crystal inserted inside the vacuum chamber on the path of the 800 nm fundamental radiation allowed the generation of 400 nm pulses while maintaining sufficient temporal and spatial overlap of 800 and 400 nm fields in the preformed plasmas. Notice that even only a small conversion efficiency (~5%) into the 400 nm radiation allowed the generation of the lower-order even harmonics alongside with the odd ones (Fig. 14, dash-dotted curves). Even harmonics generation up to H14 were observed. The seemingly relatively small yield of low-order harmonics (H6 to H9) was caused by a weaker sensitivity of the MCP detector for wavelengths above 100 nm.

The conversion efficiency of even harmonics in the case of TCP was higher than of odd harmonics in the case of SCP, despite a very low pulse energy of the 400 nm radiation with respect to the 800 nm one (~1 : 20). As it was underlined in [73] that in the case of two-color pumping stronger harmonics generation is possible due to the formation of a quasi-linear field, the selection of the short quantum path component which has a denser electron wave packet, and a higher ionization rate compared to SCP. The orthogonally polarized second field also participates in the modification of the trajectory of the accelerated electrons from being two-dimensional to three-dimensional, which may lead to a removal of the medium symmetry. With suitable control of the relative phase between the fundamental and the second harmonic radiation, the latter field enhances the short path contribution, resulting in a clean spectrum of harmonics. One can see that even at a very small ratio of 400 and 800 nm pulse energies the influence of the weak field was sufficient to strongly modify the whole harmonic spectrum compared to the single color pumping case.

Notice the relative weaker H12 compared to H10 and H14. This heterogeneity in the even harmonic yields was caused by group velocity dispersion in the 0.4 mm thick BBO crystal, which causes a notable delay between the 400 and 800 nm pulses at the output of the crystal in the case of 30 fs pulses. Each 0.1 mm of BBO causes ~19 fs delay between the driving (800 nm) and second harmonic (400 nm) waves. Thus only a small part of the second harmonic overlaps with the pulse duration of the driving fundamental 800 nm pulse. This causes a further decrease in the influence of the second harmonic field on the whole pattern of harmonic distribution. On the other hand, this second harmonic pulse generates relatively strong low-order odd harmonics: $H5_{400\,nm}$ which corresponds to $H10_{800\,nm}$, and $H7_{400\,nm}$ which corresponds to $H14_{800\,nm}$, see Fig. 14. An introduction of either positive or negative chirp in the femtosecond pulses by varying the distance between gratings in the compressor led to an increase of the pulse duration and a better overlap of the two orthogonally polarized pulses in the plasma. However, in that case, a decrease of the intensity of the driving pulse led to a general decrease of the whole harmonic yield.

The peculiarity of the gelatin plasma emission and TCP-induced harmonic spectra was the proximity of some ionic transitions of gelatin with the wavelengths of even harmonics, see H8 and the nearby emission lines of gelatin lines in the case of CdS QD (Fig. 14b) and ZnS QD (Fig. 14c) plasmas. Neither enhancement nor suppression of this harmonic generated in

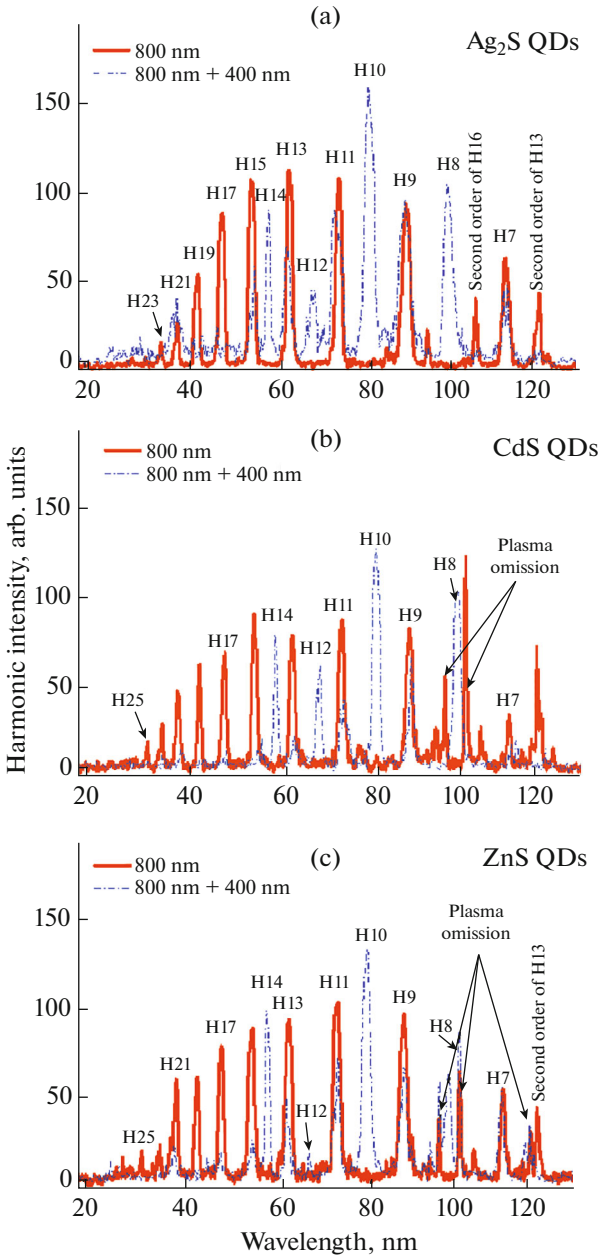

Fig. 14. Two-color (800 nm + 400 nm, dash-dotted blue line) and single-color (800 nm, full red line) pump induced harmonic spectra from Ag_2S (a), CdS (b), and ZnS (c) QDs at optimal delays between the heating and driving pulses for each species. Reproduced from R. A. Ganeev, G. S. Boltaev, V. V. Kim, K. Zhang, A. I. Zvyagin, M. S. Smirnov, O. V. Ovchinnikov, P. V. Redkin, M. Wöstmann, H. Zacharias, and C. Guo, Opt. Express **26**, 35013 (2018).

both plasmas was observed. These studies showed that the proximity of strong emission lines and harmonics does not necessarily lead to a variation of the harmonic yield.

The estimates of conversion efficiency were carried out using the comparison with known results from other plasmas). In the case of silver plasma at similar conditions, almost equal conversion efficiencies with regard to ZnS was observed in the range of 40–110 nm. By knowing the conversion efficiency from previous measurements of harmonic generation in the plasmas produced on the surface of bulk Ag (4×10^{-6}), the conversion efficiency in ZnS QD plasmas, which was 7 times higher than in bulk ZnS plasma, was calculated to be ~3×10^{-5}.

4.4. Analysis of Plasma HHG in QDs

The reviewed experiments have two key features: ablation by nanosecond pulses and QDs-containing targets. So, the observed enhanced HHG conversion efficiency can have three origins: HHG from QDs, HHG from larger concentrations of neutral atoms and HHG enhancement due to the interaction of QDs with atoms. Present studies show that particles with sizes of the order of a few nanometers can effectively generate high-order harmonics. HHG directly from QDs has not yet been studied theoretically, but a simulation of HHG from small clusters showed the increased HHG yield under the assumption of possible recombination of an electron on different atoms in the cluster. The cutoff harmonics were also enhanced much more strongly than the plateau harmonics, which is in good agreement with our experimental results in the case of ZnS QDs (Fig. 12).

Early experiments with larger nanostructures (carbon nanotubes, nanoparticles of metals and semiconductors, and other agglomerates of relatively large sizes (20–80 nm)) have shown both merits and drawbacks of this method for increasing the HHG efficiency. An increased recombination cross section of the parent particle with the accelerated electron which, in the case of relatively large particle sizes, may result in an increased number of harmonic emitters is accompanied by a reduced number of atoms located on their surface. In traditional gas HHG, therefore, fewer atoms are involved in the generation of the harmonics because the atoms located inside the nanoparticles are unlikely to participate in HHG. As a consequence, the amount of harmonic generation processes per single atom falls short for large nanoparticles. Another mechanism for HHG is found in solids [74]. In this case, the electron is excited to a conduction band, and different channels including intraband and interband processes are proposed for the actual generation of the harmonics [75, 76]. HHG in solids could also become relevant for nanoparticles. From this perspective, QDs may act as an intermediate material between atoms and solid states. As already mentioned, earlier studies have revealed benefits in using small nanoparticles for HHG. The exact number of atoms in the particle for optimal generation of coherent XUV radiation remains a puzzle, despite the fact that, to date, a large number of experiments with gas clusters, as well as ablated nanoparticles, were conducted.

Laser ablation induced HHG spectroscopy of semiconductors can reveal the resonance-induced enhancement of some harmonic orders in the XUV range as well as the cluster-induced growth of harmonic yield. The latter assumption has been demonstrated in [77] where the third and fifth harmonic generation of an IR (1064 nm) pulsed laser has been studied in ablation plasmas of the wide band-gap compounds (CdS and ZnS). Their investigation of the temporal behavior of the harmonic generation has revealed the presence of three distinct compositional populations in these plasmas. Species ranging from atoms to nanometer-sized particles have been identified as emitters, and their NLO properties could be studied separately because they appear at well-separated times in the interaction region with the driving laser pulse. In their experiment, it was found that at earlier times (<500 ns for the distance chosen for the driving beam) mostly atomic species are responsible for harmonic generation, while clusters mostly contribute at later times (>1 μs).

The harmonic generation in such plasma can prove or disapprove the role of the complex composition of ablated species in this process. A signature which would reveal the nature of the emitters is the growth of harmonics emission with the time delay with respect to the ablation laser pulse. This delay is converted to the time of propagation of QDs or clusters to the interaction region with the ultrashort driving pulse. It was suggested in [78] that, in the case of a thermalized ablation plume, the average arrival times can be assigned to different cluster sizes. The delay at which the harmonic yield reaches its maximum should scale as a square root of the atomic or molecular weight of the constituents. The ejection of lighter clusters from QDs allows them to reach the region of the driving beam earlier as heavier species.

Therefore QDs comprising of n molecules should appear in the interaction zone $n^{0.5}$ times later compared to single atoms, molecules, or ions of the sulfides. The present HHG studies reveal that for bulk target ablation the maximum yield from single CdS and ZnS molecules occurred at a delay of about ~300–400 ns. The corresponding QDs allowed efficient generation at about 400–500 ns delay, which is a similar delay as in the former case. Further, attempts to observe HHG at the delays of up to 50 μs, the expected delay for thermalized larger nanoparticles, did not show any harmonic emission. Thus our studies show that QDs arrive at the area of interaction with the femtosecond laser beam notably earlier than one would expect for a thermalized ablation plume. In other words, all metal sulfide molecules in QDs acquire, from the very beginning, a similar kinetic energy and spread out from the surface with velocities approximately similar to that of single metal sulfide molecule ablating from bulk material. This conclusion reconciles the similarity in the optimal delays for HHG from bulk and QD targets of the same material.

It was suggested in [77] that a similar average kinetic energy $E = mv^2/2$ could characterize all plasma components of the same elemental composition. Thus the average arrival time assigned to the particles containing different amount of identical molecules will be approximately the same. The reviewed studies have confirmed this assumption. The difference in "optimal" delays between heating and driving pulses is related with the difference in the velocities of particles, which depends on the atomic masses of the components of molecules.

One can expect from this assumption the arrival of ZnS ions, atoms and QDs in the area of interaction with driving beam at $(M_{Ag_2S}:M_{ZnS})^{0.5} \sim 1.59$ times earlier with regard to Ag_2S-containing particles taking into account the ratio between the atomic weights of these two molecules ($M_{Ag_2S}:M_{ZnS} \approx 2.54$). Once we compare the "optimal" delays for these two species, their ratio (400 ns : 250 ns = 1.6) becomes close to the above estimates. Thus, one can assume that above rule properly explains the dynamics of material spreading out from the ablated target, once one analyzes the particles' movement during laser ablation at relatively moderate fluencies (5–20 J cm^{-2}) of heating nanosecond pulses.

As already mentioned, an increase of the recombination cross section for QDs with respect to atoms or single molecules can enhance the HHG efficiency in multi-particle plasmas. An additional cause for strong harmonics generation from QDs compared to single atoms or ions could be the higher concentration of neutral metal sulfide molecules inevitably accompanying the presence of multi-particle species. QDs present the extreme case of solid-state density in a very small volume. Compared to solids, they still do not absorb all the HHG radiation produced inside them due to their very small thickness. QDs can further improve phase-matching conditions for harmonics generated from atoms and ions using compensation of free-electron dispersion of the driving pulse by dispersion of clusters.

A new method for the analysis of multi-particle plasma formations using two laser sources for HHG in the laser ablation can be considered as a promising approach to materials science. Its application will expand the possibilities of optimizing HHG in laser-induced plasma plumes, allow the implementation of new approaches to the study of large molecules and clusters undergoing ablation, and will significantly increase the range of objects of study compared to HHG in gases. Thus, the method presented is not only an alternative approach in generating stronger coherent XUV radiation but rather can serve as a tool for various spectroscopic and analytical applications.

5. SUMMARY

In this review, we have discussed different nonlinear optical properties of QDs. Particularly, the optical limiting in $Cd_{0.5}Zn_{0.5}S$ + erythrosine associates was analyzed. The stabilization of propagated radiation at the level of 0.65 mJ of 532 nm, 40 ps pulses was discussed. We have reviewed NLO processes in the solutions containing $Cd_{0.5}Zn_{0.5}S$ QDs and their associates with three types of dyes using 1064 nm and 532 nm pulses, to determine the mechanisms of observed optical limiting. These studies allowed calculating NLO parameters associated with the two-photon absorption, saturable absorption, reverse saturable absorption, as well as nonlinear refraction in those solutions. It was shown that the nonlinear refraction of studied solutions was due to the Kerr nonlinearity in the field of picosecond laser pulses. In the meantime, the nonlinear absorption was attributed to the two-photon absorption, saturable absorption, and reverse saturable absorption.

We analyzed NLO properties of QDs in order to determine the effect of influence of the low-order nonlinearity on the high-order one. In particular, the generation of high-order harmonics in those QDs can be performed with the use of femtosecond and picosecond laser pulses. We have discussed the quantitative analysis of NLO parameters of QD + dye associates. Particularly, we have analyzed the normalized transmittances of alloyed QDs in the case of the open and closed aperture Z-scan schemes and discussed the potential role of nonlinear absorption during high-order harmonic studies using those species. The analysis of these dependences allowed calculating the basic low-order optical nonlinearities (i.e. nonlinear refraction indices and nonlinear absorption coefficients).

The novelty of the reviewed studies is related with the potential applications of alloyed quantum dots in their future applications as the media suitable for efficient high-order harmonic generation and creation of the sources of coherent extreme ultraviolet radiation. To define best conditions of plasma formations containing such alloyed quantum dots for harmonic generation one has to carefully study the low-order NLO processes in these species. This knowledge will help to restrict the impeding processes influencing the conversion efficiency of infrared pulses towards the short wavelength region. Thus the performed calculations of the nonlinear refractive and absorptive properties of alloyed quantum dots allow the application of those features for optimization of higher-order NLO processes, such as high-order harmonic generation.

Further, we have analyzed NLO properties of 4 nm Ag_2S QD suspensions using 60 fs and 200 ps pulses of 800 nm and 400 nm radiation. At 400 nm, 200 ps pump pulses, those QDs have demonstrated large nonlinear absorption (up to $\beta \approx 10^{-3}$ cm W^{-1}) comparable with the highest reported values using nanosecond laser irradiation at 532 nm, and relatively strong nonlinear refraction ($\gamma = -6 \times 10^{-9}$ cm^2 W^{-1}). The relatively high nonlinear absorption coefficients of QDs (up to 8.8×10^{-8} cm W^{-1}) and moderate nonlinear refractive indices (up to 3×10^{-12} cm^2 W^{-1}) were obtained using 800 nm, 60 fs pump. We have shown that the nonlinear absorption of Ag_2S QDs can be more effectively used for OL of femtosecond pulses compared to the toluene, which has large nonlinear absorption. The analysis of transient absorption of QDs allowed determination of the time constants attributed to electron-phonon (1.7 ps) and phonon-phonon (6.9 ps) processes.

We systematically analyzed the dynamics of variations of the sign of nonlinear refraction at different pulse widths and wavelengths of probe radiation. Overall, our studies of nonlinear absorption and refraction of Ag_2S QDs may allow definition of the optimal conditions of excitation of these QDs for high-order harmonic generation during formation of plasma plumes containing such species. The large RSA may indirectly indicate the possibility of some transitions to be involved in the growth of nonlinear susceptibility and the enhancement of single harmonic or group of harmonics during frequency conversion of ultrashort laser pulses interacting with such QDs.

Finally, we have analyzed the possibility and conditions of using quantum dots as efficient emitters for high-order harmonics generation by 30 fs pulses using optimally delayed heating and driving laser pulses. A comparison of HHG using QDs and ablation of solid-state targets for the same materials (Ag_2S, ZnS, and CdS) was carried out. In the case of QDs, the conversion efficiency into harmonics is higher despite the lower concentration of these species in the plasma compared to the concentration of molecules and ions for bulk ablation. The observed increase of HHG conversion efficiency could be caused by a larger concentration of harmonic emitters and the specific properties of QDs, particularly their plasmonic properties. The maximum HHG conversion efficiency is achieved much earlier than one would expect from the kinetic model of QDs spreading out from the target surface. Therefore similar velocity distributions of molecules and QDs of these metal sulfides are assumed in the ablation process.

REFERENCES

1. F. Chen, S. Dai, T. Xu, X. Shen, C. Lin, Q. Nie, C. Liu, and J. Heo, Chem. Phys. Lett. **514**, 79 (2011).
2. R. E. Bailey and S. Nie, J. Am. Chem. Soc. **125**, 7100 (2003).
3. L. W. Tutt and A. Kost, Nature (London, U.K.) **356**, 225 (1992).
4. N. Venkatram, D. N. Rao, and M. A. Akundi, Opt. Express **13**, 867 (2005).
5. R. Karimzadeh, H. Aleali, and N. Mansour, Opt. Commun. **284**, 2370 (2011).

6. D. Sharma, B. P. Malik, and A. Gaur, J. Opt. **17**, 045502 (2015).
7. A. D. Lad, P. P. Kiran, D. More, G. R. Kumar, and S. Mahamuni, Appl. Phys. Lett. **92**, 043126 (2008).
8. P. Işık, A. Karatay, H. Gul Yaglioglu, A. Elmali, U. Kürüm, A. Ateş, and N. Gasanly, Opt. Commun. **288**, 107 (2013).
9. I. L. Bolotin, D. J. Asunskis, A. M. Jawaid, Y. Liu, P. T. Snee, and L. Hanley, J. Phys. Chem. C **114**, 16257 (2010).
10. R. A. Ganeev, M. Morita, A. I. Ryasnyansky, M. Baba, D. Rau, H. Fujii, M. Suzuki, M. Turu, and H. Kuroda, Opt. Spectrosc. **97**, 530 (2004).
11. R. A. Ganeev, M. Baba, A. I. Ryasnyansky, M. Suzuki, and H. Kuroda, Opt. Spectrosc. **99**, 668 (2005).
12. M. S. Smirnov, O. V. Ovchinnikov, I. G. Grevtseva, A. I. Zvyagin, A. S. Perepelitsa, and R. A. Ganeev, Opt. Spectrosc. **124**, 681 (2018).
13. R. A. Ganeev, Opt. Spectrosc. **122**, 250 (2017).
14. R. A. Ganeev, Opt. Spectrosc. **123**, 351 (2017).
15. T. D. Donnelly, T. Ditmire, K. Neuman, M. D. Perry, and R. W. Falcone, Phys. Rev. Lett. **76**, 2472 (1996).
16. J. W. G. Tisch, T. Ditmire, D. J. Fraser, N. Hay, M. B. Mason, E. Springate, J. P. Marangos, and M. H. R. Hutchinson, J. Phys. B **30**, L709 (1997).
17. C. Vozzi, M. Nisoli, J.-P. Caumes, G. Sansone, S. Stagira, S. de Silvestri, M. Vecchiocattivi, D. Bassi, M. Pascolini, L. Poletto, P. Villoresi, and G. Tondello, Appl. Phys. Lett. **86**, 111121 (2005).
18. H. Ruf, C. Handschin, R. Cireasa, N. Thiré, A. Ferré, S. Petit, D. Descamps, E. Mével, E. Constant, V. Blanchet, B. Fabre, and Y. Mairesse, Phys. Rev. Lett. **110**, 083902 (2013).
19. R. A. Ganeev, M. Suzuki, M. Baba, M. Ichihara, and H. Kuroda, J. Phys. B **41**, 045603 (2008).
20. R. A. Ganeev, M. Suzuki, M. Baba, M. Ichihara, and H. Kuroda, J. Opt. Soc. Am. B **25**, 325 (2008).
21. R. A. Ganeev, P. A. Naik, H. Singhal, J. A. Chakera, M. Kumar, M. P. Joshi, A. K. Srivastava, and P. D. Gupta, Phys. Rev. A **83**, 013820 (2011).
22. F. Wu, G. Zhang, W. Tian, L. Ma, W. Chen, G. Zhao, S. Cao, and W. Xie, J. Opt. A **10**, 075103 (2008).
23. V. V. Danilov, A. S. Panfutova, A. I. Khrebtov, and T. S. Titova, Opt. Spectrosc. **118**, 94 (2015).
24. D. Yu, K. Du, J. Zhang, F. Wang, L. Chen, M. Zhao, J. Bian, Y. Feng, and Y. Jiao, New J. Chem. **38**, 5081 (2014).
25. V. G. Klyuev, D. V. Volykhin, O. V. Ovchinnikov, and S. I. Pokutnyi, J. Nanophoton. **10**, 033507 (2016).
26. X. Zhong, Y. Feng, W. Knoll, and M. Han, J. Am. Chem. Soc. **44**, 13559 (2003).
27. A. J. Peter and C. W. Lee, Chin. Phys. B **21**, 087302 (2012).
28. G. S. Boltaev, D. J. Fu, B. R. Sobirov, M. S. Smirnov, O. V. Ovchinnikov, A. I. Zvyagin, and R. A. Ganeev, Opt. Express **26**, 13865 (2018).
29. R. A. Ganeev, A. I. Zvyagin, O. V. Ovchinnikov, and M. S. Smirnov, Dyes Pigments **149**, 236 (2018).
30. S. Valligatla, K. K. Haldar, A. Patra, and N. R. Desai, Opt. Laser Technol. **84**, 87 (2016).
31. W. Wu, Z. Chai, Y. Gao, D. Kong, F. He, X. Meng, and Y. Wang, Opt. Mater. Express **7**, 1547 (2017).
32. R. A. Ganeev, A. I. Ryasnyansky, M. K. Kodirov, S. R. Kamalov, and T. Usmanov, Opt. Spectrosc. **93**, 789 (2002).
33. R. A. Ganeev, A. I. Ryasnyansky, and H. Kuroda, Opt. Spectrosc. **99**, 1006 (2005).
34. I. Gur, N. A. Fromer, M. L. Geier, and A. P. Alivisatos, Science (Washington, DC, U. S.) **310**, 462 (2005).
35. V. M. N. Tessler, M. Kazes, S. Kan, and U. Banin, Science (Washington, DC, U. S.) **295**, 3 (2002).
36. D. V. Talapin and C. B. Murray, Science (Washington, DC, U. S.) **310**, 86 (2005).
37. M. Bruches Jr., M. Moronne, P. Gin, S. Weiss, and A. P. Alivisatos, Science (Washington, DC, U. S.) **281**, 2013 (1998).
38. R. A. Ganeev, A. I. Ryasnyansky, and T. Usmannov, Opt. Quantum Electron. **35**, 211 (2003).
39. G. S. Boltaev, B. Sobirov, S. Reyimbaev, H. Sherniyozov, T. Usmanov, M. S. Smirnov, O. V. Ovchinnikov, I. G. Grevtseva, T. S. Kondratenko, H. S. Shihaliev, and R. A. Ganeev, Appl. Phys. A **122**, 999 (2016).
40. Z. Zeng, C. S. Garoufalis, A. F. Terzis, and S. Baskoutas, J. Appl. Phys. **114**, 023510 (2013).
41. Y. P. Sun, J. E. Riggs, K. B. Henbest, and R. B. Martin, J. Opt. Soc. Am. B **9**, 481 (2000).
42. R. Karimzadeh, H. Aleali, and N. Mansour, Opt. Commun. **284**, 2370 (2011).
43. M. Sheik-Bahae, A. A. Said, T. H. Wei, D. J. Hagan, and E. W. van Stryland, IEEE J. Quantum Electron. **26**, 760 (1990).
44. L. W. Liu, S. Y. Hu, Y. P. Dou, T. H. Liu, J. Q. Lin, and Y. Wang, Beilstein J. Nanotechnol. **6**, 1781 (2015).
45. G. Fan, S. Qu, Q. Wang, C. Zhao, L. Zhang, and Z. Li, J. Appl. Phys. **109**, 023102 (2011).
46. R. A. Ganeev, A. I. Ryasnyansky, A. T. Stepanov, and T. Usmanov, Opt. Quantum Electron. **36**, 949 (2004).
47. H. Zeng, Y. Yang, X. Jiang, G. Chen, J. Qiu, and F. Gan, J. Cryst. Growth **280**, 516 (2005).
48. R.A. Ganeev, M. Suzuki, M. Baba, M. Ichihara, and H. Kuroda, J. Appl. Phys. **103**, 063102 (2008).
49. R. A. Ganeev, G. S. Boltaev, R. I. Tugushev, and T. Usmanov, Appl. Phys. B **100**, 571 (2010).
50. Y. Fu, R. A. Ganeev, C. Zhao, K. S. Rao, S. K. Maurya, W. Yu, K. Zhang, and C. Guo, Appl. Phys. B **125**, 1 (2019).
51. A. Sahu, L. Qi, M. S. Kang, D. Deng, and D. J. Norris, J. Am. Chem. Soc. **133**, 6509 (2011).
52. H. Aleali and N. Mansour, Optik **127**, 2485 (2016).
53. J. Sun, W. Yu, A. Usman, T. T. Isimjan, S. Dgobbo, E. Alarousu, K. Takanabe, and O. F. Mohammed, J. Phys. Chem. Lett. **5**, 659 (2014).
54. W. J. Mir, A. Swarnkar, R. Sharma, A. Katti, K. V. Adarsh, and A. Nag, J. Phys. Chem. Lett. **6**, 3915 (2015).
55. M. Sheik-Bahae, D. Hutchings, D. J. Hagan, and E. W. van Stryland, IEEE J. Quantum Electron. **27**, 1296 (1991).
56. J. Etchepare, G. Grillon, J. P. Chambaret, G. Hamoniaux, and A. Orszag, Opt. Commun. **63**, 329 (1987).

57. T. Kawazoe, H. Kawaguchi, J. Inoue, O. Haba, and M. Ueda, Opt. Commun. **160**, 125 (1999).
58. L. Jing, S. V. Kershaw, Y. Li, X. Huang, Y. Li, A. L. Rogach, and M. Gao, Chem. Rev. **116**, 10623 (2016).
59. F. Nan, F.-M. Xie, S. Liang, L. Ma, D.-J. Yang, X.-L. Liu, J.-H. Wang, Z.-Q. Cheng, X.-F. Yu, L. Zhou, Q.-Q. Wang, and J. Zeng, Nanoscale **8**, 11969 (2016).
60. R. A. Ganeev, H. Singhal, P. A. Naik, J. A. Chakera, M. Tayyb, A. K. Srivastava, T. S. Dhami, M. P. Joshi, A. Singh, R. Chari, S. R. Kumbhare, R. P. Kushwaha, R. A. Khan, and P. D. Gupta, Opt. Spectrosc. **108**, 787 (2010).
61. R. A. Ganeev, L. B. Elouga Bom, and T. Ozaki, Opt. Spectrosc. **108**, 970 (2010).
62. H. Singhal, R. A. Ganeev, P. A. Naik, J. A. Chakera, U. Chakravarty, H. S. Vora, A. K. Srivastava, C. Mukherjee, C. P. Navathe, S. K. Deb, and P. D. Gupta, Phys. Rev. A **82**, 043821 (2010).
63. L. W. Liu, S. Hu, Y. P. Dou, T. H. Liu, J. Q. Lin, and Y. Wang, Beilstein J. Nanotechnol. **6**, 1781 (2015).
64. G. S. Boltaev, B. Sobirov, S. Reyimbaev, H. Sherniyozov, T. Usmanov, M. S. Smirnov, O. V. Ovchinnikov, I. G. Grevtseva, T. S. Kondratenko, H. S. Shihaliev, and R. A. Ganeev, Appl. Phys. A **122**, 999 (2016).
65. Z. Zeng, C. S. Garoufalis, A. F. Terzis, and S. Baskoutas, J. Appl. Phys. **114**, 023510 (2013).
66. R. Karimzadeh, H. Aleali, and N. Mansour, Opt. Commun. **284**, 2370 (2011).
67. R. A. Ganeev, G. S. Boltaev, V. V. Kim, K. Zhang, A. I. Zvyagin, M. S. Smirnov, O. V. Ovchinnikov, P. V. Redkin, M. Wöstmann, H. Zacharias, and C. Guo, Opt. Express **26**, 35013 (2018).
68. C. Hutchison, R. A. Ganeev, T. Witting, F. Frank, W. A. Okell, J. W. G. Tisch, and J. P. Marangos, Opt. Lett. **37**, 2064 (2012).
69. C. M. Kim and C. H. Nam, J. Phys. B **39**, 3199 (2006).
70. T. Pfeifer, L. Gallmann, M. J. Abel, D. M. Neumark, and S. R. Leone, Opt. Lett. **31**, 975 (2006).
71. R. A. Ganeev, H. Singhal, P. A. Naik, I. A. Kulagin, P. V. Redkin, J. A. Chakera, M. Tayyab, R. A. Khan, and P. D. Gupta, Phys. Rev. A **80**, 033845 (2009).
72. R. A. Ganeev, V. V. Strelkov, C. Hutchison, A. Zaïr, D. Kilbane, M. A. Khokhlova, and J. P. Marangos, Phys. Rev. A **85**, 023832 (2012).
73. I. J. Kim, G. H. Lee, S. B. Park, Y. S. Lee, T. K. Kim, C. H. Nam, T. Mocek, and K. Jakubczak, Appl. Phys. Lett. **92**, 021125 (2008).
74. S. Ghimire, A. D. DiChiara, E. Sistrunk, P. Agostini, L. F. DiMauro, and D. A. Reis, Nat. Phys. **7**, 138 (2011).
75. O. Schubert, M. Hohenleutner, F. Langer, B. Urbanek, C. Lange, U. Huttner, D. Golde, T. Meier, M. Kira, S. W. Koch, and R. Huber, Nat. Photon. **8**, 119 (2014).
76. G. Vampa, C. R. McDonald, G. Orlando, D. D. Klug, P. B. Corkum, and T. Brabec, Phys. Rev. Lett. **113**, 073901 (2014).
77. R. de Nalda, M. López-Arias, M. Sanz, M. Oujja, and M. Castillejo, Phys. Chem. Chem. Phys. **13**, 10755 (2011).
78. M. Oujja, J. G. Izquierdo, L. Bañares, R. de Nalda, and M. Castillejo, Phys. Chem. Chem. Phys. **20**, 16956 (2018).